# *ROSAT* OBSERVATIONS OF FIVE POOR GALAXY CLUSTERS WITH EXTENDED RADIO SOURCES

STEPHEN M. DOE, MICHAEL J. LEDLOW, AND JACK O. BURNS

Department of Astronomy, Box 30001/Department 4500, New Mexico State University, Las Cruces, New Mexico 88003-8001
Electronic mail: sdoe@head-cfa.harvard.edu, mledlow@nmsu.edu, jburns@nmsu.edu

RICHARD A. WHITE

NASA/Goddard Space Flight Center, Space Data and Computing Division, Code 932, Greenbelt, Maryland 20771
Electronic mail: rwhite@jansky.gsfc.nasa.gov

*Received 1994 December 6; revised 1995 March 14*

## ABSTRACT

We present the results of deep *ROSAT* PSPC observations of the poor clusters MKW2, N79-299A, S49–128, S49–132, and S49–140. These poor clusters all contain extended radio sources, generally with a bent, head–tail (HT) morphology. It had been previously thought that HTs should only be found in rich clusters, which have sufficiently high intracluster medium (ICM) densities and velocity dispersions for effective ram pressure bending of the radio jets. We have found that the X-ray emission associated with these poor clusters is generally quite clumpy and asymmetrical. Often, the clumps are associated with subgroups or individual galaxies, as well as with extended regions around the radio sources. Our results also indicate that there is a continuum of X-ray properties from poor to rich clusters. In many respects, poor clusters seem to be a low-mass extension of rich clusters. We find that these poor clusters have baryon fractions ranging from 1% to 25%. Also, the radio sources within these clusters are probably thermally confined by the ICM. Although four of our clusters have central X-ray luminosity excesses, the implied cooling times are longer than a Hubble time. We interpret the central X-ray luminosity excesses as unresolved galaxy emission. We hypothesize that these poor clusters have recently collapsed out of large, loose clouds of galaxies. We believe that many of the poor cluster properties are understandable in light of this hypothesis. First, four of these five clusters are embedded within larger Zwicky clusters. This may indicate that these large Zwicky clusters act as "incubators" of poor clusters. Second, the observed flat, broad velocity distributions may reflect the velocities associated with the larger-scale systems from which we believe that these poor clusters have collapsed. Third, some of these galaxies (such as NGC 4061, within N79-299A) show signs of interactions with neighboring galaxies with large relative velocities (≈850 km/s). Fourth, the observed ICM densities, coupled with velocity distributions which are suggestive of unrelaxed systems, and the peculiar velocities of the radio galaxies may explain the ram pressure bending of the radio jets in the HTs. 

## 1. INTRODUCTION

Poor clusters of galaxies are defined as those clusters which have Abell (1958) richness class <0 (Bahcall 1980). Richness class 0 clusters have at least 30 members in the magnitude range of $m_3$ to $m_3+2$, where $m_3$ is the apparent magnitude of the third brightest galaxy. To this day, Abell's catalog is used as the primary source list of rich clusters. Abell clusters have been extensively studied through the years, yet only ~5% of all galaxies are found within rich clusters (Dressler 1984). According to Dressler, over ~50% of all galaxies are found in poor clusters of galaxies. Thus, a very large fraction of the mass in the universe is probably located in poor groups. An understanding of the physical conditions in poor clusters is vital for studies of galaxy evolution as well as large-scale structure and cosmological models.

A number of poor clusters have been catalogued over the past two decades. Morgan *et al.* (1975, hereafter referred to as MKW) and Albert *et al.* (1977, hereafter referred to as AWM) defined a sample of poor groups containing cD galaxies (sometimes referred to as Yerkes poor clusters). It had been previously thought that cDs occurred only in rich clusters. Hickson (1982) searched through the Palomar Observatory Sky Survey (POSS) red prints for poor, compact groups of galaxies. These compact groups were required to have at least four members within three magnitudes of the brightest galaxy. These groups were also required to be dense (within the smallest circle that contained the centers of all the galaxies in the group, the average surface brightness had to be 26.0 mag per arcsec$^2$ or brighter). Since the cores of rich clusters can approach this degree of compactness, these groups also had to be isolated from other (external) galaxies which were within three magnitudes of the brightest galaxy of the group. Hickson identified 100 such groups. The Hickson, MKW, and AWM catalogs were basically chosen by eye. Turner & Gott (1976), on the other hand, used an automated "friends-of-friends" approach to define a sample of groups by electronically searching through Zwicky's (1961–68) Catalog of Galaxies and Clusters of Galaxies (CGCG) for overdensities down to a limiting magnitude of $m_V=14$. Another important sample of groups was compiled by

 0004-6256/95/110(1)/46/22/$0.90  

Huchra & Geller (1982) from the CfA red-shift survey, to a limiting magnitude of $m_B = 13.2$. In this catalog, 92 groups were located from number density enhancements using both position and velocity information.

White *et al.* (1995) used a "friends-of-friends" technique similar to that of Turner & Gott (1976) to compile a catalog of over 600 poor clusters. These poor clusters were selected optically, from a computer version of the CGCG, down to a limiting magnitude of 15.7. In order to be included in their catalog, a cluster was required to have a surface density enhancement of at least $10^{4/3}$ (corresponding to a volume density enhancement of 100), and contain at least three galaxies from the CGCG. Although the entire CGCG was searched, only regions of the sky North and South of $\pm 40°$ galactic latitude were considered to be sufficiently free of the effects of galactic absorption to be suitable for statistical studies. The result was a catalog of over 600 poor clusters (with $\sim$450 North and South of $\pm 40°$ galactic latitude), including some MKW and AWM clusters, Hickson groups, and a few Abell clusters. VLA 20 cm imaging of a subsample of 139 of these poor clusters was reported by Burns *et al.* (1987). This subsample consisted of poor clusters with at least three members in the CGCG, with surface density enhancements of at least $10^{5/3}$ (i.e., the next increment up from the base level surface density enhancement of the sample), and which could be fit into the constraints of the observational program. Because these clusters were chosen on nonintrinsic criteria (i.e., there was insufficient observing time to look at all the clusters in crowded regions of the sky), they are representative of the total catalog.

One surprising result of the Burns *et al.* survey was the frequency with which head–tail (HT) radio sources occur within these poor clusters. HT radio sources, particularly narrow-angle tails (NATs), are thought to form from galaxies moving through the ICM with sufficient velocity to bend the radio jets via ram pressure (O'Dea 1985). Eilek *et al.* (1984) and O'Dea (1985) have calculated that for rich clusters, relative velocities of $\sim$1000 km/s are required to bend jets into HT morphologies (see also Sec. 5). The average ram pressure for a cluster is $\rho_{\rm ICM}\sigma_v^2$ (where $\rho_{\rm ICM}$ is the ICM density and $\sigma_v$ is the cluster velocity dispersion). Using values from Price *et al.* (1991), the average ram pressure for a poor cluster is a factor of $\sim$100 lower than the average ram pressure in rich clusters. This suggests that HTs should occur much less frequently in poor clusters than in rich clusters.

However, HTs do, in fact, seem to occur just as frequently in poor as in rich clusters. We compared the Burns *et al.* poor cluster sample to a complete VLA 20 cm radio survey of 117 Abell clusters with red-shift $z < 0.06$ (Ledlow & Owen 1995). (The poor clusters of the Burns *et al.* survey are also within $z < 0.06$.) For the Abell clusters, we have computed an estimate of the total number of galaxies surveyed by summing the richness counts from Abell (1958). The percentage of HT sources found in these rich clusters was calculated by taking the ratio of the total number of HTs to the galaxy counts. For the poor clusters, we counted the number of surveyed galaxies down to a magnitude limit similar to that used by Abell, but with a search radius of 0.5 Mpc. This is a more appropriate search radius, as these groups are relatively compact. We then computed the percentage of HTs in poor clusters. In both samples, we found that $\approx$0.6% of all galaxies exhibit HT morphologies. Ledlow & Owen (1995) found that in rich clusters, $\approx$2% of all cluster galaxies are Fanaroff & Riley Type I (1974) radio sources. Thus, the distorted HT sources comprise about 25% of all radio galaxies. Given the similarity in the radio luminosity function in both rich and poor galaxy density environments (Auriemma *et al.* 1977; Fanti 1984; Ledlow 1994), it appears that bent HTs are equally common in both poor and rich clusters.

Venkatesan *et al.* (1994) chose four of the ten HTs from the Burns *et al.* survey for further detailed imaging with the VLA. These radio galaxies were observed using the VLA A and C configurations at wavelengths of 20 and 6 cm. Venkatesan *et al.* find that each of these four radio sources are strikingly similar in radio morphology and general properties to tailed sources found in rich clusters. NGC 4061 and NGC 7503, with U-shaped structure virtually identical to NGC 1265 in Perseus, were examined in detail (see Figs. 2 and 4). It was found that the sizes and shapes, the degree of jet collimation, jet opening angles, and jet luminosities as a fraction of the total luminosity were quite similar to rich cluster NATs. This would seem to imply that the physical conditions in the environment around NATs must be similar in both rich and poor clusters. However, given the large inferred differences between rich and poor clusters, the similar ram pressure environments must arise from a different mechanism in the poor groups. Burns *et al.* (1994a,b,c) have suggested that the evolutionary state of these poor clusters and their relationship to a larger-scale structure may play an important role in understanding these observations.

Extended radio emission from individual cluster galaxies acts as a probe of the cluster gaseous environment because the radio plasma is probably confined and shaped by the ICM. Burns *et al.* (1981b) presented X-ray observations of 11 4C radio sources in poor clusters. In ten of these clusters, the X-ray emission was centered on the radio galaxy. Burns *et al.* concluded that the radio sources were confined by the X-ray emitting gas, and that the cluster gas is the crucial link between cluster environment and radio emission. More recently, Burns *et al.* (1994a,b,c) have carried out correlative studies of the *Einstein* archives and the *ROSAT* All-Sky Survey with the Abell catalog, and found that 75% of the radio galaxies in a sample of rich clusters are within 5′ of significant X-ray peaks. Burns *et al.* hypothesized that the local gas environments of radio galaxies play a more crucial role in determining radio galaxy characteristics than the global properties of clusters.

A relatively small number of poor clusters were imaged by the *Einstein* X-ray satellite. Price *et al.* (1991) reported the results of *Einstein* X-ray observations of 25 poor clusters, comparing their X-ray, optical, and radio properties with those of rich clusters. Price *et al.* found that both the optical properties (such as richness and velocity dispersion) and the X-ray properties (such as X-ray luminosity, core radius, and ICM density) are continuous between poor and rich clusters (i.e., the ranges in the values for these properties overlap between poor and rich clusters). Kriss *et al.* (1983) presented the results of *Einstein* imaging of poor clusters containing cD

TABLE 1. Dates and lengths of observations.

| Cluster | Date | Integration Time (seconds) | $N_s^a$ | $N_b^b$ |
|---|---|---|---|---|
| MKW2 | 20 Nov. 1992 | 11464 | 565 | 1535 |
| N79-299A | 12-13 June 1991 | 15991 | 1437 | 9593 |
| S49-128 | 14-15 Aug. 1993 | 16319 | 510 | 1359 |
| S49-132 | 16-19 June 1992, 15 Dec. 1992 | 13390 | 3690 | 521 |
| S49-140 | 1-2 Aug. 1993 | 13295 | 1635 | 7520 |

[a]Number of source counts in the region within 0.33 Mpc of the cluster center.
[b]Number of background counts in the region within 0.33 Mpc of the cluster center.

galaxies. Kriss *et al.* also found that cDs in rich and poor clusters possess many optical and X-ray morphological similarities (e.g., cooling flows), suggesting a similar origin for dominant galaxies in rich and poor clusters.

Recent *ROSAT* observations have increased the number of poor clusters with X-ray data. For example, 12 of Hickson's (1982) compact groups (HCGs) have been detected from the *ROSAT* All-Sky Survey (Henriksen & Mamon 1994). Pointed observations of the NGC 2300 (Mulchaey *et al.* 1993) and NGC 5044 (David *et al.* 1994) poor clusters, and HGC 62 (Ponman & Bertram 1993) have also been made. Mulchaey *et al.* found that the baryon fraction of the NGC 2300 group is about 4%, implying that some poor clusters may have a higher percentage of dark matter than typical rich clusters. However, for this same poor group, Henriksen & Mamon's (1994) reanalysis found a baryonic fraction of 20%. This discrepancy may in part be due to difficulties in accurately measuring the X-ray background in the cluster. Saracco & Ciliegi (1995) searched the *ROSAT* public archives, available as of March 1994, and found eight HCGs that had been observed for >3000 s and have apparent X-ray detections. The X-ray emission for two of them (HCG 16 and HCG 44) originate from point sources coincident with galaxies in the groups. The X-ray emission for three of the groups (HCG 62, HCG 92, and HCG 97) is clearly extended and is probably due to hot intracluster gas. In these cases, the temperature of the ICM is ≈0.9 keV. It is unclear if the X-ray emission for the remaining three groups (HCG 4, HCG 12, and HCG 15) originates from diffuse gas or from point sources. Saracco and Ciliegi claim low $(Z/Z_\odot \sim 0.1-0.2)$ metal abundances for the gas in these groups, a result which is consistent with an ICM composed of primordial gas. Pildis *et al.* (1995) also analyzed *ROSAT* PSPC observations of 13 compact groups (12 HCGs and the NGC 2300 group). Pildis *et al.* report that eight of these groups have extended X-ray emission, and for four of these groups find gas temperatures of ≈1 keV. Seven of the eight groups with extended X-ray emission have spiral fractions of less than 50%. Also, Pildis *et al.* report baryon fractions of 5%–19% within these groups. To date, a number of poor clusters with a significant ICM have been observed.

In this paper, we present the results of deep *ROSAT* pointed observations of five poor clusters from the Burns *et al.* (1987) survey. These five poor clusters all contain extended, generally distorted radio sources that are larger than the *ROSAT* Position Sensitive Proportional Counter (PSPC) beam. The radio source may also act as an additional probe of the surrounding ICM. By observing both the overall cluster gas distribution and the environments around radio galaxies within these clusters, we hope to understand how the NATs and the clusters were formed, and to study the overall properties of these clusters.

This paper is organized in the following manner. In Sec. 2, we describe the PSPC spatial and spectral data analysis. In Sec. 3, we discuss the observed properties of each cluster. In Sec. 4, we compare these observations to rich cluster properties, as well as to other poor clusters. In Sec. 5 we present an interpretation of these data which may account for the existence of NATs in these poor clusters. In Sec. 6, we summarize the results and present our conclusions. We use $H_0 = 75$ km s$^{-1}$ Mpc$^{-1}$ throughout this paper.

## 2. DATA REDUCTION TECHNIQUES

We have obtained *ROSAT* PSPC pointed observations of the clusters MKW2, N79-299A, S49–128, S49–132, and S49–140. MKW2 is one of the poor groups originally identified by Morgan *et al.* (1975). All five poor groups occur in the listing of poor clusters in Burns *et al.* (1987). These poor clusters were observed from 1991–1993, for total integration times ranging from 12–16,000 s. Table 1 lists the dates and lengths of these observations.

The *ROSAT* X-ray telescope (XRT) consists of a four-fold nested Wolter mirror configuration. The XRT covers an energy range of 0.07 to 2.4 keV. The detector used in our observations, the PSPC, is most sensitive to X rays from 0.5–2.0 keV, making it ideal for the study of cooler (~1 keV) poor groups, as opposed to hotter rich clusters. The PSPC has a spatial resolution of 25″ in the focal plane at an energy of 0.93 keV (MPE 1991). In the central 20′ of the field, the spatial resolution is energy dependent. At larger off-axis angles, the spatial resolution is dominated by the XRT and is energy independent. Also, the PSPC has limited energy resolution, with $\Delta E/E = 0.43(E/0.93)^{-0.5}$ (FWHM) over the entire sensitive area of the PSPC (MPE 1991). The energy band can be conveniently divided into two bands separated by a broad carbon K$\alpha$ absorption band (0.20–0.83 keV) in the plastic window of the PSPC.

In Sec. *2.1*, we discuss the techniques used in producing the X-ray images. We describe the methods used for spectral fitting in Sec. *2.2*. In Sec. *2.3* we show how the basic X-ray properties of the clusters were calculated.

### 2.1 Spatial Reductions

The analysis of PSPC observations of point sources is reasonably straightforward. Provided the source is centered in the field, event selection and the vignetting and exposure corrections can be performed relatively easily. Additionally, a fairly accurate estimate of the X-ray background can be determined from an annulus surrounding the source. The 'xspatial' package within the PROS analysis software contains the standard programs used to reduce point source X-ray data. However, a proper treatment of PSPC observations of extended sources is inherently more complex. The telescope and detector quantum efficiencies vary over the field of view, and the background rates and sensitivity of the detector depend on both the energies and positions of the incoming photons. Thus, these corrections are ultimately much more important when one is interested in extracting the maximum amount of information from the extended, diffuse emission at large, off-axis radii.

Snowden *et al.* (1994) describe a set of procedures recommended for the reduction of PSPC observations of extended sources. We have used a $\beta$-release version of Snowden's software package along with some routines in PROS. We used the eight energy bands defined by Snowden *et al.* to produce X-ray maps for these clusters. (Because of the limited spectral resolution of the PSPC, it was decided that a small number of broad energy bands should be defined for the study of the spatial properties of extended objects.) We chose to use a broadband covering the energy range 0.44–2.04 keV, which involved combining many of the Snowden bands. This choice allowed us to exclude a significant fraction of the background counts ($\sim$50%), especially at very soft energies, while sacrificing only $\sim$10% of the source counts. Thus, the signal-to-noise ratio was substantially increased. We now briefly describe our approach for reducing PSPC data, based upon the discussion in Snowden *et al.* (1994).

The heart of the problem is to determine the background across the field of view of the PSPC as a function of energy. Snowden *et al.* have identified five different components to the noncosmic background. The particle induced background (PB) is caused by high-energy charged particles and $\gamma$ rays that can penetrate the detector. After-pulses (AP) often occur after large pulse-height events and can cause ghost images in the detector. APs are believed to be due to negative ion formation in the detector. The solar X-ray background (SB) arises from solar X rays scattered by the Earth's atmosphere. Finally, there are short-term and long-term enhancements (STEs and LTEs). STEs are caused by sporadic events such as auroral X rays and produce high count rates lasting from minutes to hours. The origins of LTEs are more mysterious. LTEs vary on a time scale of 1–2 days and are strongest in the soft (<0.3 keV) bands. The routines described by Snowden *et al.* allow one to model each of these sources of the X-ray background, and to subtract their contributions in each energy band as a function of position on the detector. Once the spatially dependent background contributions are removed, the flat cosmic background can be estimated easily from blank regions in the image.

For our data, we first examined the lightcurve for valid time intervals. Selections were made based on master-veto rates (i.e., particle background contamination). Periods in which the master-veto count rate was greater than 170 counts $s^{-1}$ were eliminated. Also, all events occurring within 0.35 ms of a previous event were removed to reduce afterpulse contamination. Times of very obvious STEs (which manifest themselves as sharply falling or rising enhancements at the start or end of observation intervals) were also removed. The result was a list of acceptable time intervals which contained uncontaminated data.

The background count rates were cast into sky coordinates and were subtracted from the data. The vignetted background components are scaled by the exposure map in each energy band and added to the nonvignetted background before the final subtraction. The exposure correction is then applied to the background subtracted data to produce the final image. By using this procedure, the signal-to-noise for the diffuse emission is increased by a factor of $\sim$5, so that we can more accurately define the extent and properties of the diffuse emission in our final images.

### 2.2 Spectral Reductions

For the spectral analysis, we used principally the standard PROS 'XSPECTRAL' package. We used the time-filter determined in Sec. *2.1* to construct new photon event files, from which we extracted our spectra.

Next, we defined the source and background regions for each cluster. The source region was determined by a circle of radius 330 kpc centered on the brightest X-ray clump. Other point sources were removed from the source region. We found the FWHMs of the emission associated with each point source, and used three times the FWHM as the diameter of a circle surrounding each point source. The background region was defined by either an annulus or a number of boxes outside the source region.

The package 'XSPECTRAL' contains the tasks necessary for extracting the spectrum. The photons from the specified source region were binned into 34 pulse-height invariant (PI) channels. Photons from the first 11 PI channels (0.11–0.28 keV) were not used when making fits to the spectrum because of low source counts and signal to noise. Photons from the background regions were binned in the same manner, and normalized by the area of the source region. The extracted spectrum was then fit by an absorbed Raymond–Smith thermal plasma model which was convolved with the calibrated telescope and instrument response [see, e.g., Fig. 1(c)]. From the best-fit solutions, we derived values for the gas temperature of each cluster. Within PROS, the column density can also be left as a free parameter, but, except in the case of S49–132, we found that the derived column densities were virtually unconstrained anyway. Thus, we fixed $N_H$ at the Stark *et al.* (1992) value and we let the temperature vary freely when fitting each spectrum.

Initially, the metal abundances were fixed at 30% solar, as metal abundance must remain a fixed parameter within PROS. However, the metal abundances for these clusters are

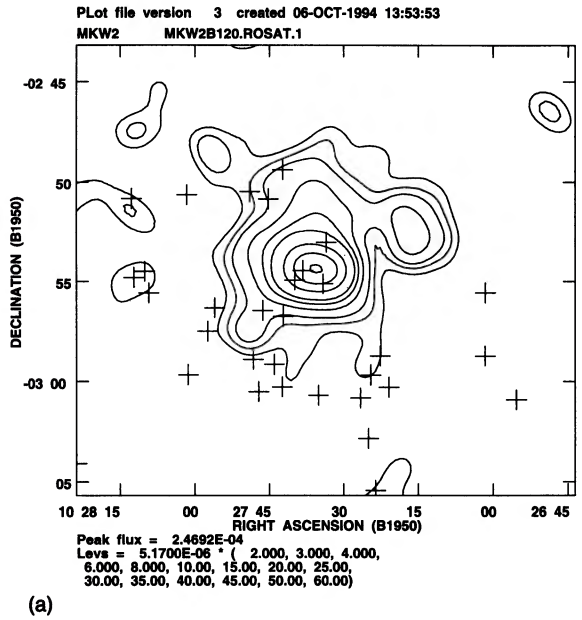


(a)

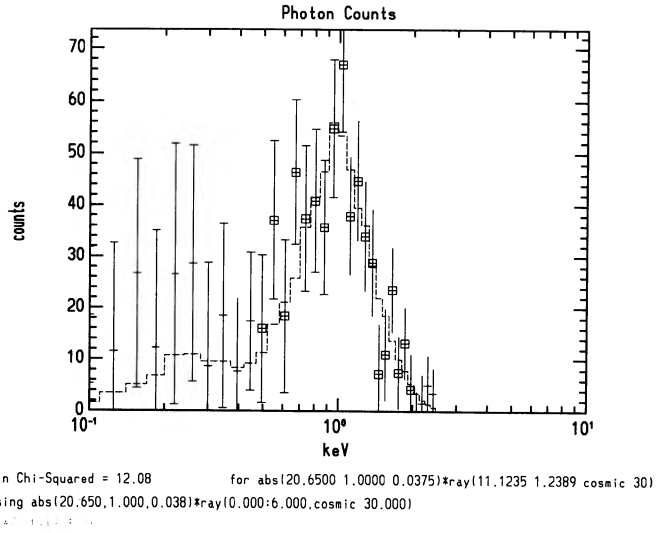


(c)

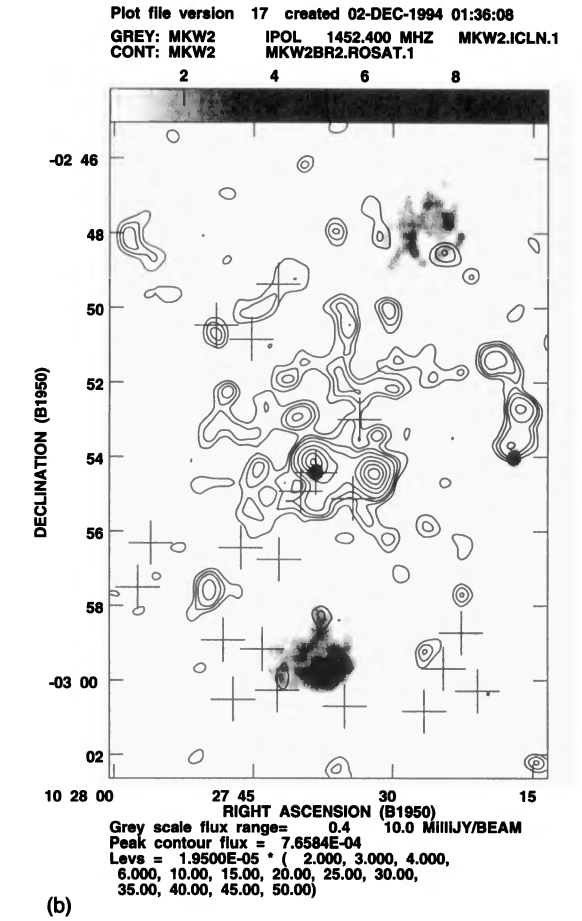


(b)

FIG. 1. Spatial and spectral data for MKW2. (a) Contour map of the X-ray emission, smoothed with a 2′ Gaussian. The peak flux is $2.47\times10^{-4}$ counts/s/arcmin$^2$, and $\sigma=5.17\times10^{-6}$ counts/s/arcmin$^2$. The contour levels are 2, 3, 4, 6, 8, 10, 15, 20, 25, 30, 35, 40, 45, 50, and 60$\sigma$. The crosses denote galaxy positions. (b) High-resolution map of X-ray and radio emission. The grey scale shows the radio source and the contours again show the X-ray emission, this time smoothed with a 30″ Gaussian. The grey scale ranges from 0.4 to 10 mJy/beam. The peak contour flux is $7.66\times10^{-4}$ counts/s/arcmin$^2$, and $\sigma=1.95\times10^{-5}$ counts/s/arcmin$^2$. The contour levels are 2, 3, 4, 6, 10, 15, 20, 25, 30, 35, 40, 45, and 50$\sigma$. The crosses show the galaxy positions. (c) The X-ray spectrum. The $x$ axis shows energy in keV and the $y$ axis shows counts per channel. The boxes with error bars show the data, and the dashed line is the best-fit Raymond–Smith model. The data were fit for $E>0.284$ keV.

not known *a priori*. Thus, for each cluster, we performed additional spectral fits with the metal abundance fixed at 10%, 20%, 30%, and 40% solar. The $\chi^2$ statistic for the best fit to each cluster does change as metal abundance changes. But, are any of these fits *significantly* better than any of the others? In other words, does an abundance of 10% solar result in a significantly better fit than an abundance of 40% solar?

Since S49–132 has the most source counts ($N_s=3690$), we used this cluster as the "best case" for examining the quality of the fits as the metal abundance was varied. We carried out a series of model fits using the Goddard Space Flight Center XSPEC package (v8.50), in which metal abundance is allowed as a free parameter. In the first four fits, $N_H$ was fixed at the Stark *et al.* value, $4.7\times10^{20}$ cm$^{-2}$, the metal abundance was fixed to 10%, 20%, 30%, and 40%, respectively, and the temperature varied freely. In the last fit, $N_H$ was again fixed, and both metal abundance and temperature were allowed to vary freely. Table 2 lists the metal abundance, derived temperature $\chi^2$ and number of degrees of

TABLE 2. Spectral fit parameters for S49–132.

| Fit | $Z/Z_\odot$ | $kT$ (keV) | $\chi^2$ | $\nu^a$ |
|---|---|---|---|---|
| Fit 1 | 0.1 | $2.16^{+1.05}_{-0.53}$ | 27.0 | 20 |
| Fit 2 | 0.2 | $1.94^{+0.81}_{-0.42}$ | 22.7 | 20 |
| Fit 3 | 0.3 | $1.91^{+0.74}_{-0.37}$ | 20.3 | 20 |
| Fit 4 | 0.4 | $1.98^{+0.73}_{-0.37}$ | 19.5 | 20 |
| Fit 5 | $0.4^{+0.4}_{-0.2}$ | $2.02^{+0.86}_{-0.42}$ | 19.5 | 19 |

[a] $\nu$ is the number of degrees of freedom in the fit.

freedom for each fit; the errors listed for the free parameters correspond to the 90% confidence limits.

To more rigorously test the quality of the fits listed in Table 2, we also performed the F test. The F test is a measure of the statistical significance of the difference between two statistics, $\chi_1^2$ and $\chi_2^2$, where the ratio of the reduced $\chi^2$'s follows the F distribution (Bevington 1969). Thus,

$$F=\frac{\chi_1^2/\nu_1}{\chi_2^2/\nu_2}, \tag{1}$$

where $\nu_1$ and $\nu_2$ are the numbers of degrees of freedom corresponding to $\chi_1^2$ and $\chi_2^2$. One can use the F distribution to calculate the probability that the two $\chi^2$'s are not significantly different. A variation of the F test allows one to test the quality of the fit with an additional degree of freedom, where

$$F_\chi=\frac{\chi^2(n-1)-\chi^2(n)}{\chi^2(n)/(N-n-1)}. \tag{2}$$

Here $\chi^2(n-1)$ corresponds to a fit with $n-1$ parameters, $\chi^2(n)$ corresponds to a fit with $n$ parameters, and $N-n-1$ is the number of degrees of freedom for the latter fit. This is a measure of how significantly the additional term has improved the value of the reduced $\chi^2$, and should be small when the additional term does not significantly improve the fit. If $F>F_\chi$, the F distribution can be used to calculate the probability $P(F>F_\chi)$ that the reduction in $\chi^2$ is not statistically significant.

The results of the F test are shown in Table 3. Each of the first four fits was compared to the last fit, and $F$, $F_\chi$, and $P(F>F_\chi)$ were calculated. In the last fit, the abundance was $0.4^{+0.4}_{-0.2}$. Thus, even for the cluster with the highest number of source counts, the constraints that can be placed upon the metal abundance are very broad. Also, the F test indicates that when the abundance was fixed at 30% solar and at 40% solar, adding the metal abundance as a free parameter did not improve the quality of the fit significantly. This makes sense, since in these fits, the metal abundance was fixed to a value within the 90% confidence levels quoted above.

Since we cannot constrain the metal abundance to within better than the broad range 0.2–0.8, and given the results of the F test, we have fixed $Z/Z_\odot$ to a nominal value of 30%, which is typical of clusters of galaxies (Butcher & Stewart 1991). We have used the PROS spectral fitting routines, with metal abundance fixed to 30%, to produce Figs. 1–5(c). In Table 4, the derived values for $kT$ (with 90% errors) and the Stark *et al.* values for $N_H$ are given, as well as the $\chi^2$ and number of degrees of freedom.

### *2.3 Poor Cluster Data Analysis*

We produced final images of the five clusters using the procedure outlined in Sec. *2.1*. The images were smoothed with Gaussians of FWHM=30″, 1′, and 2′. The purpose of using the 30″ convolution was to identify small-scale structure. The more heavily smoothed images were used to examine the overall lower surface-brightness distribution of the X-ray emission associated with each cluster. Figures 1–5 show contour maps of the X-ray emission for each cluster. Part (a) in these figures display the largest scale X-ray emission, convolved with a 2′ Gaussian. Part (b) of these figures show 30″-smoothed contour maps of the X-ray emission

TABLE 3. F-test results for S49–132.

| Fits Compared[a] | $F^b$ | $F_\chi^c$ | $P(F>F_\chi)^d$ |
|---|---|---|---|
| Fits 1,5 | 0.76 | 7.33 | $1.40\times10^{-2}$ |
| Fits 2,5 | 0.91 | 3.10 | 0.09 |
| Fits 3,5 | 0.99 | 0.82 | 0.38 |
| Fits 4,5 | 0.95 | 0.05 | 0.83 |

Notes to TABLE 3

[a] Each of the first four fits is compared to the fifth, to test for the significance of adding the extra term in Fit 5.
[b] $F$ is the ratio of the reduced $\chi^2$ s.
[c] The F test for the additional term. If $F>F_\chi$, then the quality of the fit is probably not improved if the additional term (in this case, metal abundance) is allowed to vary freely.
[d] The probability that the reduction in $\chi^2$ that results from the additional term is not significant.

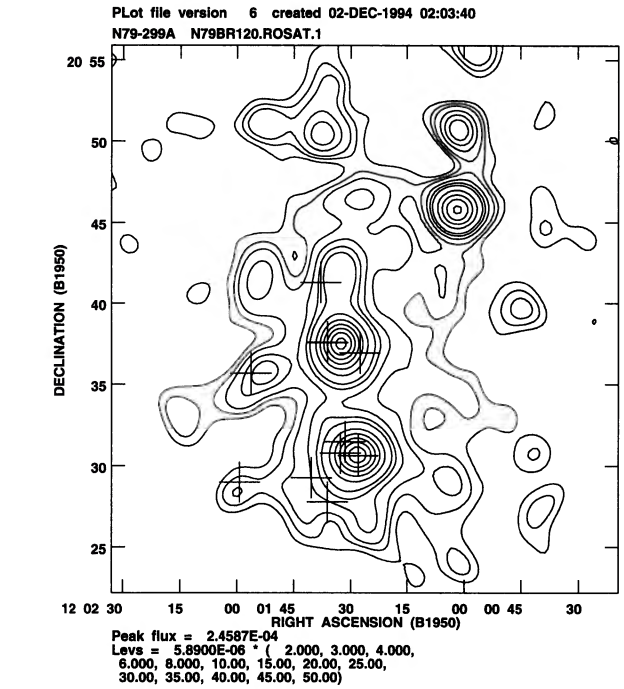


(a)

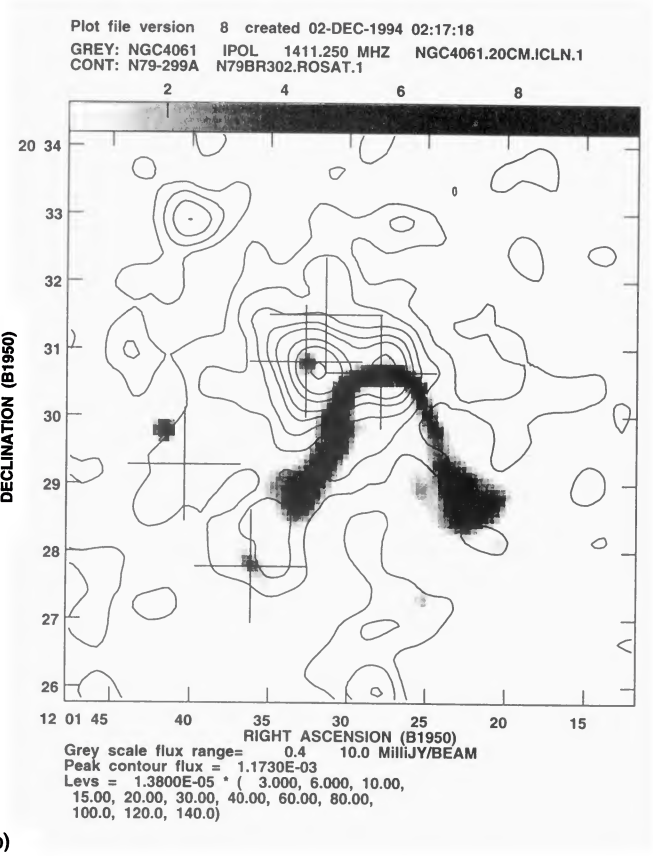


(b)

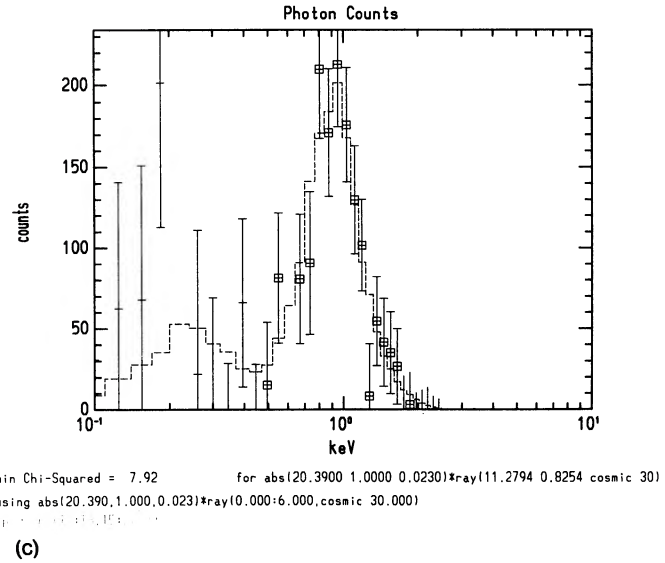


(c)

FIG. 2. Spatial and spectral data for N79-299A, as in Fig. 1. (a) The peak flux is $2.46\times10^{-4}$ counts/s/arcmin$^2$, and $\sigma=5.89\times10^{-6}$ counts/s/arcmin$^2$. The contour levels are 2, 3, 4, 6, 8, 10, 15, 20, 25, 30, 35, 40, 45, and 50$\sigma$. (b) The greyscale ranges from 0.4 to 10 mJy/beam. The peak contour flux is $1.17\times10^{-3}$ counts/s/arcmin$^2$, and $\sigma=1.38\times10^{-5}$ counts/s/arcmin$^2$. The contour levels are 3, 6, 10, 15, 20, 30, 40, 60, 80, 100, 120, and 140$\sigma$. (c) The X-ray spectrum, as in Fig. 1(c).

around the radio sources in these clusters. The first contour is $2\sigma$. The radio emission is represented as grey scale, overlayed onto X-ray contours. The crosses denote optical galaxy positions. We measured the positions of many galaxies in these clusters using the Mann measuring engine at NRAO in Socorro, NM. The positions are accurate to $\approx1''$. We measured positions on the POSS E prints for all galaxies within half a degree of the cluster center with $m_V<17$. Some of the radio maps were taken from Burns *et al.* (1987) and some from Venkatesan *et al.* (1994).

For each cluster, we also fit elliptical isophotes to the surface brightness. We used an effective radius ($r=\sqrt{ab}$) for the final profile. We allowed the ellipticity and position angle of each elliptical isophote to vary with each solution, but kept the centroid fixed on the X-ray peak. The isophotal radii were geometrically increased by 10% to keep the S/N approximately the same in each annulus. Often, multiple X-ray peaks or clumps were embedded within the diffuse emission. Our general procedure was to take the clump with the highest surface brightness as the center of the cluster emission, and to subtract out all the other discernable point sources. For each cluster, we have parametrized the X-ray surface brightness profile by fitting a King (1962) function:

$$S(r)=S_0[1+(r/r_c)^2]^{-3\beta+1/2}, \quad (3)$$

where $r_c$ is the core radius and $\beta$ is the ratio of the energy density per unit mass in the galaxies to that in the gas (e.g., Gorenstein *et al.* 1978). Table 7 lists the best-fit values for $r_c$ and $\beta$. For some of these clusters (e.g., N79-299A), the profiles are best described by an unresolved core and extended emission. In these cases, a fit was made to the outer portion of the profile with the inner few bins ignored. Such a central

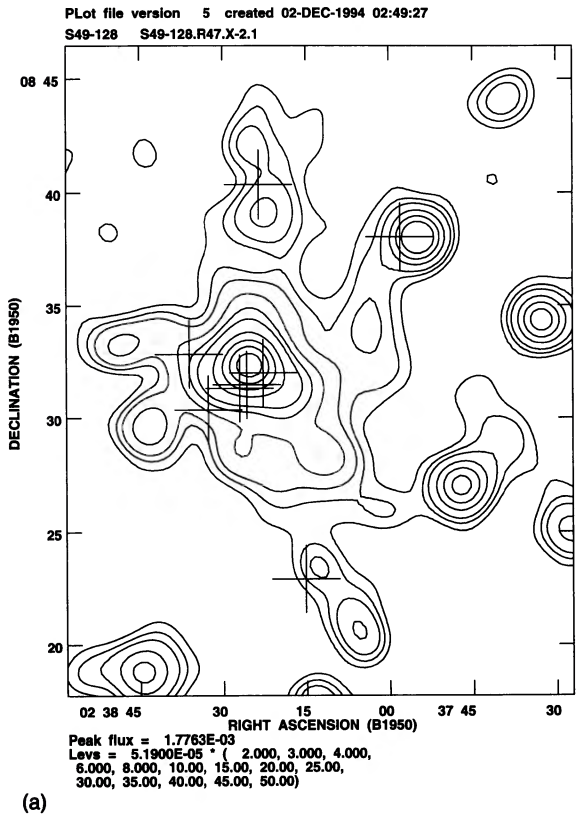


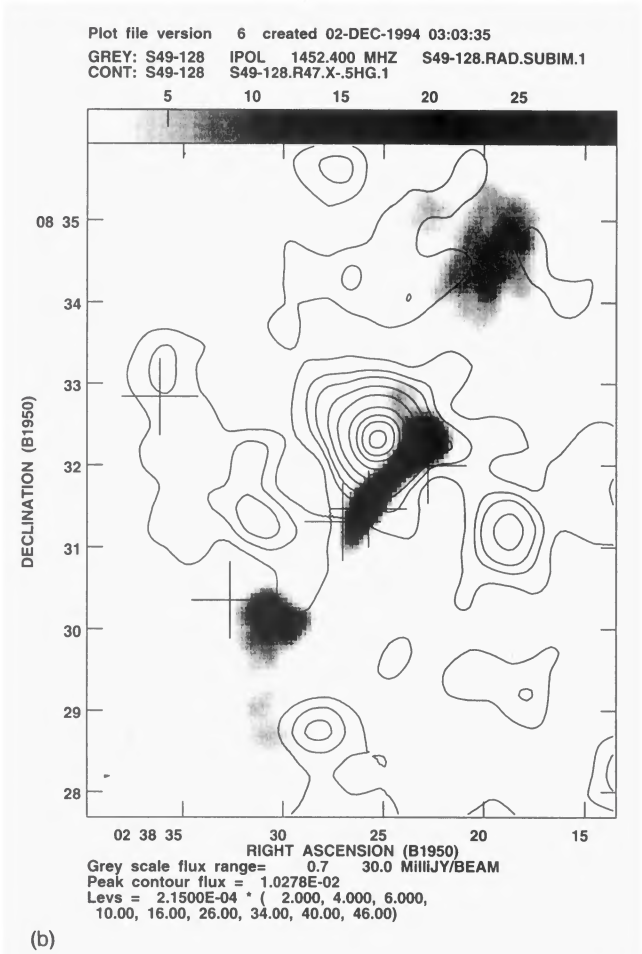


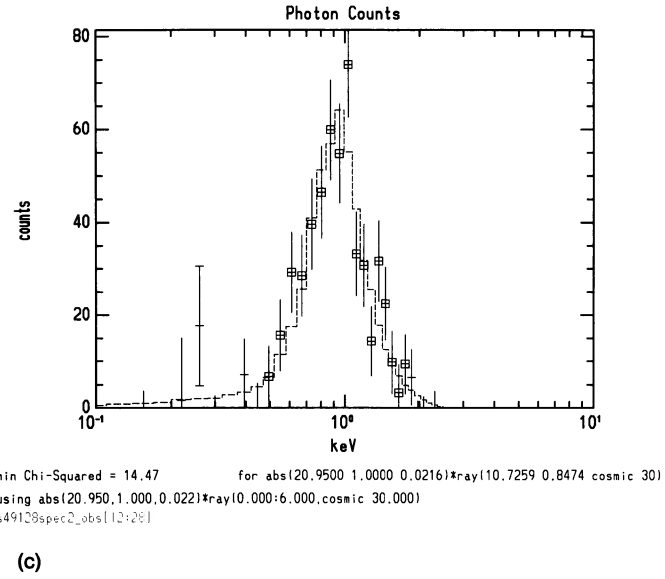


FIG. 3. Spatial and spectral data for S49–128, as in Fig. 1. (a) The peak flux is $1.77\times10^{-3}$ counts/s/arcmin$^2$, and $\sigma=5.19\times10^{-5}$ counts/s/arcmin$^2$. The contour levels are 2, 3, 4, 6, 8, 10, 15, 20, 25, 30, 35, 40, 45, and 50$\sigma$. (b) The greyscale ranges from 0.7 to 30 mJy/beam. The peak contour flux is $1.03\times10^{-2}$ counts/s/arcmin$^2$, and $\sigma=2.15\times10^{-4}$ counts/s/arcmin$^2$. The contour levels are 2, 4, 6, 10, 16, 26, 34, 40, and 46$\sigma$. (c) The X-ray spectrum, as in Fig. 1(c).

X-ray excess is often interpreted as evidence for a cooling inflow (e.g., Sarazin 1986; Fabian 1994) but may also be unresolved galaxy emission in these poor groups (see Sec. *4.4*). In Figs. 6(a)–(e), we present the best fits to the cluster profiles. Given the nature of the gas distributions in these groups, one should recognize that the King model fits are very rough, but nonetheless useful approximations of the X-ray surface brightness. The purpose of the King model parametrization is to measure quantities which can be compared to other cluster data. The total extent of the X-ray

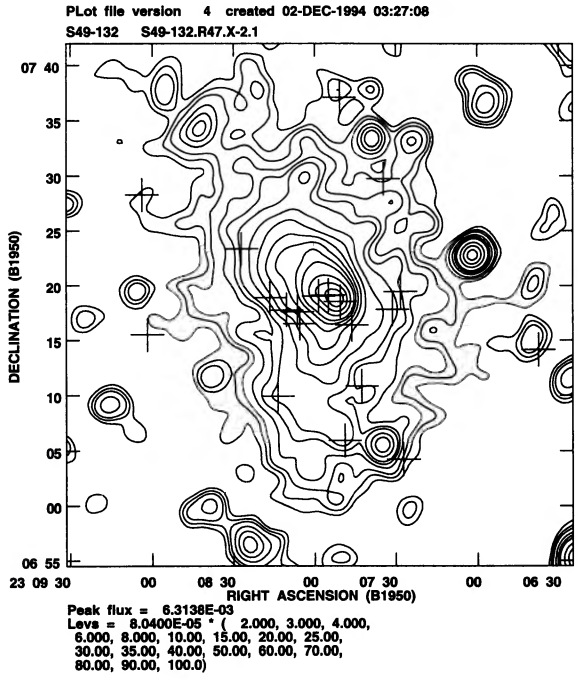


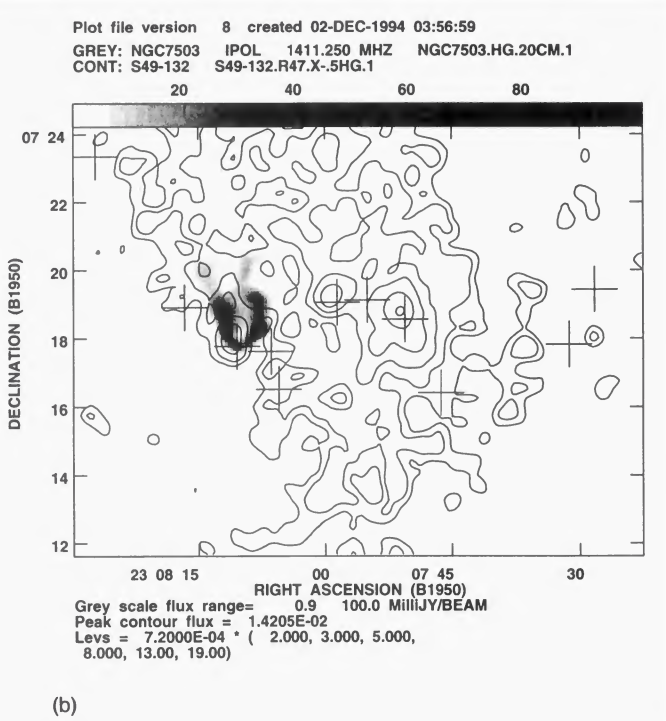


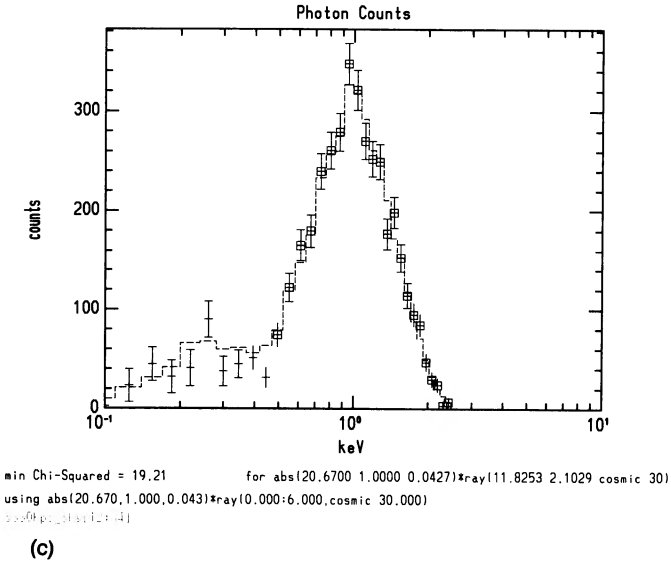


FIG. 4. Spatial and spectral data for S49–132, as in Fig. 1. (a) The peak flux is $6.31\times10^{-3}$ counts/s/arcmin$^2$, and $\sigma=8.04\times10^{-5}$ counts/s/arcmin$^2$. The contour levels are 2, 3, 4, 6, 8, 10, 15, 20, 25, 30, 35, 40, 50, 60, 70, 80, 90, and 100$\sigma$. (b) The greyscale ranges from 0.9 to 100 mJy/beam. The peak contour flux is $1.42\times10^{-2}$ counts/s/arcmin$^2$, and $\sigma=7.20\times10^{-4}$ counts/s/arcmin$^2$. The contour levels are 2, 3, 5, 8, 13, and 19$\sigma$. (c) The X-ray spectrum, as in Fig. 1(c).

emission was based upon the $2\sigma$ contour from the final images (see Table 7).

In Figs. 7(a)–7(d), we present velocity distributions for four of the poor clusters. (In the case of S49-132, there were too few published velocities from which to construct an informative histogram.) These velocities were gathered from published data via the NED and ADS databases (Helou *et al.* 1991). We used a search radius of 1.5° from the cluster center (as done in Dell'Antonio *et al.* 1994). The number of galaxies in each velocity distribution is ~20. Within a virialized cluster, the velocity distribution should be Gaussian. A non-Gaussian velocity distribution may point to interesting dynamical activity, such as a substructure within a cluster.

From the surface-brightness profiles, and constraints on the temperature from the spectral fits, we estimated the density, temperature, and pressure profiles using the deprojection technique outlined in Arnaud (1988). The emission is assumed to be spherically symmetric, so that there is a simple linear relation between the emissivity in any radial shell and the surface brightness in the corresponding circular ring. This technique also assumes that the gas is in hydrostatic equilibrium in each shell and that the ideal gas law is valid. We assume the cluster gravitational potential is described by a King function. The deprojection parameters were constrained by the average measured ICM temperatures. We note that this deprojection technique does a reasonable job in

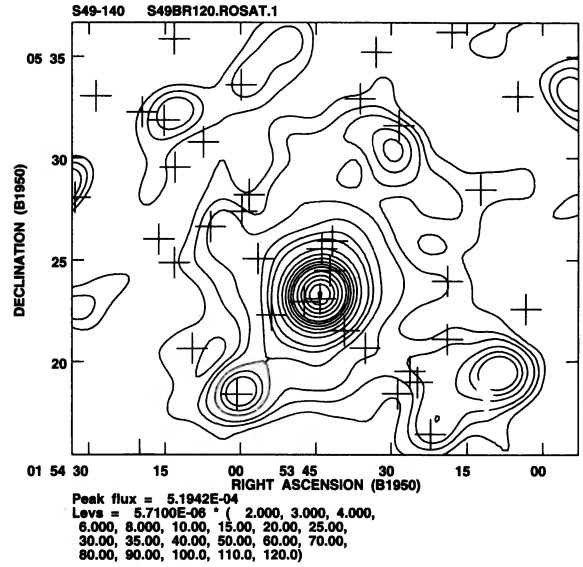


(a)

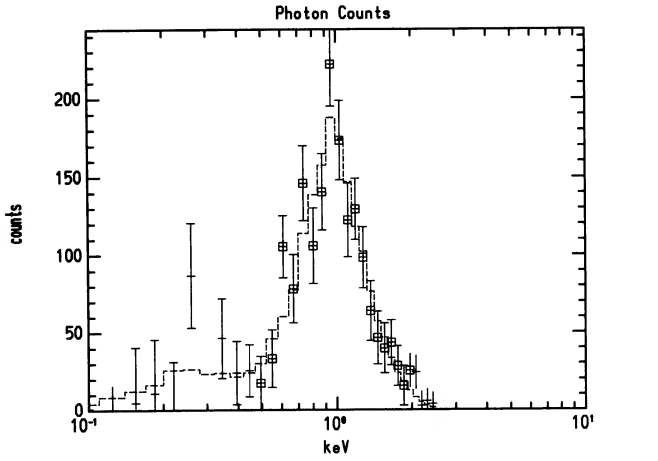


min Chi-Squared = 16.29 for abs(20.6800 1.0000 0.0188)*ray(11.3927 1.0451 cosmic 30)
using abs(20.680,1.000,0.019)*ray(0.000:6.000,cosmic 30.000)
s49_obs[12:30]

(c)

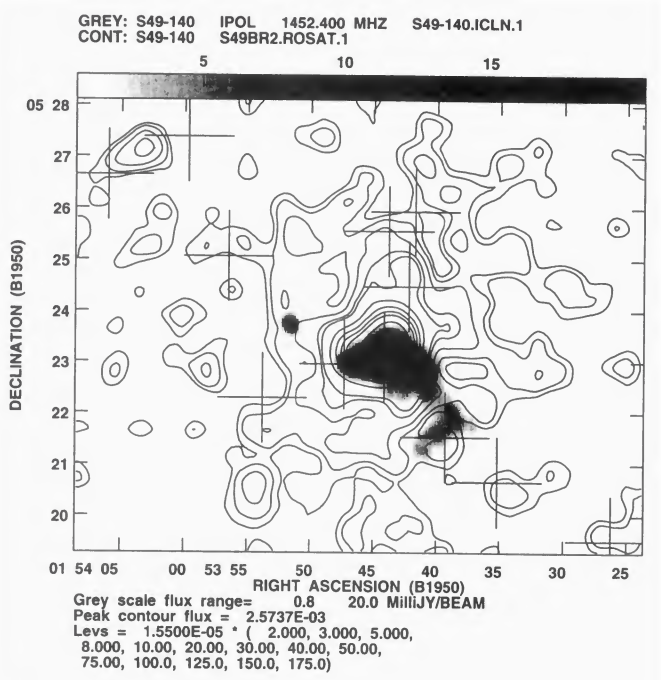


(b)

FIG. 5. Spatial and spectral data for S49-140, as in Fig. 1. (a) The peak flux is $5.19\times10^{-4}$ counts/s/arcmin$^2$, and $\sigma=5.71\times10^{-6}$ counts/s/arcmin$^2$. The contour levels are 2, 3, 4, 6, 8, 10, 15, 20, 25, 30, 35, 40, 50, 60, 70, 80, 90, 100, 110, and 120$\sigma$. (b) The greyscale ranges from 0.8 to 20 mJy/beam. The peak contour flux is $2.57\times10^{-3}$ counts/s/arcmin$^2$, and $\sigma=1.55\times10^{-5}$ counts/s/arcmin$^2$. The contour levels are 2, 3, 5, 8, 10, 20, 30, 40, 50, 75, 100, 125, 150, and 175$\sigma$. (c) The X-ray spectrum, as in Fig. 1(c).

recovering the ICM density, but is a much poorer estimate of $T(r)$ (since $\epsilon_X \propto n^2 T^{1/2}$).

## 3. COMMENTS ON INDIVIDUAL SOURCES

In Tables 5–7, we summarize the data on each of the five poor clusters. Table 5 contains the optical data on the galaxies associated with the extended radio sources. These data were gathered principally through NED and ADS. Table 6 contains information on the radio properties of each cluster taken from Burns *et al.* (1987). Table 7 summarizes the X-ray properties.

TABLE 4. Spectral fit parameters.

| Cluster | log $N_H^a$ | $kT$ (keV) | $\chi^2$ | $\nu^b$ |
|---|---|---|---|---|
| MKW2 | 20.65 | $1.24^{+2.41}_{-0.24}$ | 12.08 | 17 |
| N79-299A | 20.39 | $0.82^{+0.20}_{-0.18}$ | 7.92 | 14 |
| S49-128 | 20.95 | $0.85^{+0.20}_{-0.15}$ | 14.47 | 15 |
| S49-132 | 20.67 | $2.10^{+0.80}_{-0.50}$ | 19.21 | 20 |
| S49-140 | 20.68 | $1.04^{+0.20}_{-0.14}$ | 16.29 | 17 |

[a] Fixed to Stark *et al.* (1992) values.
[b] $\nu$ is the number of degrees of freedom in the fit.

*MKW2*: Figure 1 shows the *ROSAT* spatial and spectral data associated with this cluster. The radio source in Fig. 1(b) (i.e., the compact radio core) is identified with the brightest galaxy in the cluster, CGCG1027.6-0255. This galaxy was classified as a cD by Morgan *et al.* (1975). This relaxed double source was not imaged by Burns *et al.* (1981a) in their initial studies of the Yerkes poor clusters, due to their declination cutoff. However, Burns *et al.* (1987) presented a VLA 20 cm radio map of this source. We have reprocessed the VLA visibility data, performing several iterations of self-calibration and cleaning, to produce the somewhat higher dynamic range image shown in Fig. 1(b).

Figure 1(a) shows the extended X-ray emission associated with this cluster. The emission associated with MKW2 is the most symmetric of the five clusters. The fitted core radius (67 kpc) is the smallest in this sample, although the X-ray luminosity is about average for these poor clusters. Figure 1(b) shows a higher-resolution contour map of the X-ray

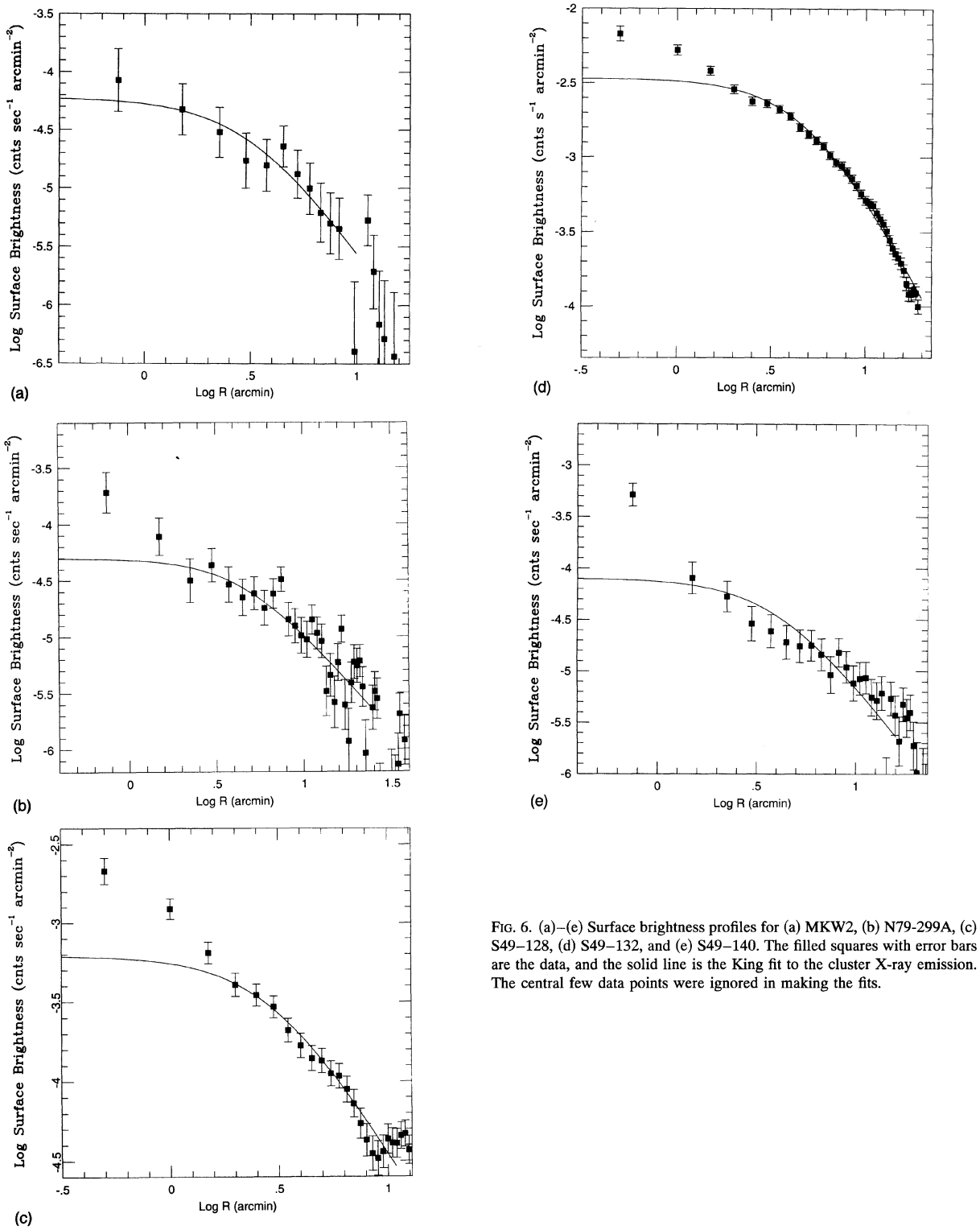


FIG. 6. (a)–(e) Surface brightness profiles for (a) MKW2, (b) N79-299A, (c) S49–128, (d) S49–132, and (e) S49–140. The filled squares with error bars are the data, and the solid line is the King fit to the cluster X-ray emission. The central few data points were ignored in making the fits.

emission superimposed on the radio grey scale. CGCG1027.6-0255 is associated with the Eastern peak of the X-ray emission. To the immediate West is another X-ray peak. We have checked its position from the POSS prints but can find no obvious optical counterpart. The nearest two cluster galaxies are several arcmin away (well beyond the errors in the X-ray position).

Figure 6(a) shows the surface-brightness profile of the cluster. This cluster does not have a central X-ray excess. The Western compact X-ray peak was subtracted from the image before constructing the surface brightness profile.

Figure 7(a) shows the velocity distribution for MKW2. There are 14 galaxies plotted in this histogram, and the distribution appears rather non-Gaussian in shape. With these

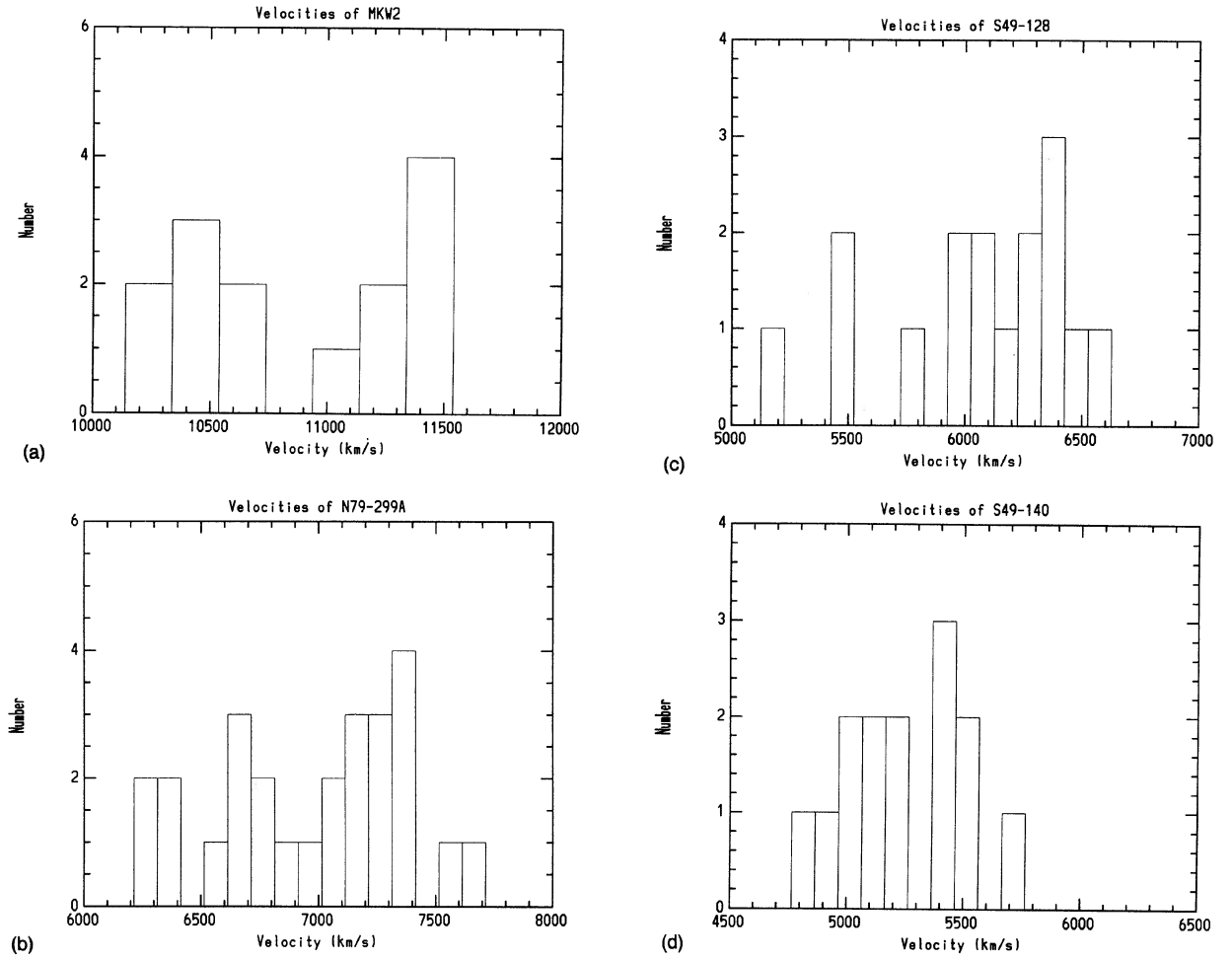


FIG. 7. (a)–(d) Velocity distributions for (a) MKW2, with 14 galaxies; (b) N79-299A, with 24 galaxies; (c) S49–128, with 16 galaxies; and (d) S49–140, with 14 galaxies. Although we are dealing with small number statistics, these velocity distributions appear flat and broad, and may suggest interesting dynamical activity within these clusters.

14 galaxies, the velocity dispersion is ~450 km/s.

Figure 1(b) shows that the radio lobes extend beyond the X-ray emitting gas. We have used the radio data to calculate the minimum pressure within the lobes (as explained in Sec. *4.5*). We have checked this value against the extrapolated thermal pressure of the X-ray gas assuming a King profile. The minimum pressure in the diffuse lobes is $1\times10^{-13}$ dyne cm$^{-2}$. From the deprojected density profile, we extrapolate a thermal pressure of $3\times10^{-13}$ dyne cm$^{-2}$. These values are within a factor of $\approx$3 of each other and are consistent with thermal confinement by the ICM, given the expected errors in our estimates.

Figure 8(a) shows the Zwicky chart of this region of the sky. MKW2 appears to be embedded within a larger contour enclosing a large concentration of galaxies. Zwicky classified this cluster as a near ($V_{\rm cluster}\leq$15,000 km/s), medium compact cluster.

*N79-299A*: The extended radio source in N79-299A is a low luminosity NAT associated with NGC 4061. This radio galaxy is a member of a poor group located within the Coma/A1367 supercluster bridge. As shown in Fig. 2(b), the radio jets curve and develop into tails, very similar to NGC 1265 (O'Dea & Owen 1986) in the Perseus cluster (Venkatesan *et al.* 1994). An unresolved radio source is associated with NGC 4065, seen to the immediate East of NGC 4061 in Fig. 2(b). Jaffe & Gavazzi (1986) published a lower resolution map of this source at 610 MHz. The 20 cm VLA radio image in Fig. 2(b) is from Venkatesan *et al.* (1994).

The extended X-ray emission associated with this cluster is shown in Fig. 2(a) to have a North–South orientation with two distinct clumps of X-ray gas and galaxies. Both clumps belong to a single poor group cataloged by Burns *et al.* (1987) and White *et al.* (1995). The higher resolution image of the southern X-ray clump in Fig. 2(b) reveals a bimodal substructure. The Eastern X-ray clump is centered on NGC 4065 and the Western clump is centered on the NAT galaxy NGC 4061, both of which are radio galaxies.

The surface-brightness profile was fit to a King profile as shown in Fig. 6(b). The clump associated with NGC 4061 was taken as the center of the emission. Other bright clumps, such as that to the North, were excluded from the fit. The NGC 4065 clump was so significant that in this case, we

TABLE 5. Properties of Zwicky galaxies within the clusters.

| Cluster/ Galaxy | mv | Type | Name | $V^a$ | $\sigma_v^b$ | $B_{gg}^c$ |
|---|---|---|---|---|---|---|
| **MKW2** | | | | | 450 | 57 |
| CGCG1027.4-0259 | 15.3 | | | | | |
| CGCG1027.6-0255 | 14.4 | | | 11260 | | |
| CGCG1028.0-0257 | 15.7 | | | | | |
| **N79-299A** | | | | | 420 | 186 |
| CGCG1201.5+2030 | 14.4 | E | NGC 4061 | 7072 | | |
| CGCG1201.5+2037 | 15.6 | | NGC 4060 | | | |
| CGCG1201.6+2027 | 15.7 | Sc | UGC 7049 | | | |
| CGCG1201.6+2030 | 14.0 | E | NGC 4065 | 6215 | | |
| CGCG1201.6+2038 | 14.4 | E | NGC 4066 | 7293 | | |
| CGCG1201.6+2042 | 14.3 | E | NGC 4070 | 7143 | | |
| CGCG1201.7+2029 | 15.6 | | NGC 4072 | | | |
| CGCG1201.7+2029 | > 17 | | | | | |
| CGCG1202.0+2028 | 14.3 | S | NGC 4076 | 6208 | | |
| CGCG1202.0+2036 | 15.4 | | NGC 4074 | 6541 | | |
| **S49-128** | | | | | 420 | 27 |
| CGCG0238.3+0832 | 15.7 | | | | | |
| CGCG0238.4+0831 | 14.8 | E | NGC 1044 | 6481 | | |
| CGCG0238.5+0830 | 14.9 | | NGC 1046 | | | |
| **S49-132** | | | | | 500[d] | 123 |
| CGCG2307.8+0718 | 15.0 | S0 | NGC 7499 | 12117 | | |
| CGCG2308.0+0718 | 15.3 | E | NGC 7501 | 12915 | | |
| CGCG2308.2+0717 | 14.9 | E | NGC 7503 | 13430 | | |
| **S49-140** | | | | | 270 | 58 |
| CGCG0153.6+0521 | 15.0 | | | 5546 | | |
| CGCG0153.7+0525 | 15.1 | | IC 1751 | | | |
| CGCG0153.7+0523 | 13.2 | E | NGC 741 | 5645 | | |
| CGCG0153.8+0523 | 14.8 | E | NGC 742 | | | |

[a]Heliocentric galaxy velocity (km/s).
[b]Cluster velocity dispersion (km/s). Velocities of cluster members obtained through the NED and ADS databases, and then velocity dispersions were computed.
[c]Spatial correlation coefficient.
[d]This value of the velocity dispersion for S49–132 was derived from the relations between $L_X$, $T$, and $\sigma_v$. When $\sigma_v = 500$ km/s was used in the deprojection analysis, the deprojected temperature profile was consistent with the observed temperature profile.

TABLE 6. Radio properties of extended sources in poor clusters.

| Cluster | Position (1950) | $S_{20}^a$ | $P_{20}^b$ | $RMT^c$ | $P_{min}^d$ |
|---|---|---|---|---|---|
| MKW2 | $10^h27^m38.3^s$ $-02°54'25''$ | 668.0 | 24.26 | Double | 0.6 |
| N79-299A | $12^h01^m27.8^s$ $20°30'40''$ | 379.0 | 23.61 | NAT | 0.3 |
| S49-128 | $02^h38^m26.0^s$ $08°31'25''$ | 1263.6 | 24.05 | Relaxed Double/WAT | 2.5 |
| S49-132 | $23^h08^m07.9^s$ $07°18'16''$ | 1661.4 | 24.81 | NAT | 3.3 |
| S49-140 | $01^h53^m47.0^s$ $05°23'00''$ | 1018.0 | 23.84 | NAT? | 1.7 |

[a]Integrated radio flux density at 20 cm, in mJy.
[b]Logarithm of the radio power at 20 cm, in W/Hz.
[c]Radio Morphological Type.
[d]Average minimum pressure within radio lobes/tails in units of $10^{-13}$ dyn cm$^{-2}$.

elected to smooth over this clump, rather than subtract it. The first two radial bins in the surface-brightness profile were not used in the fit. The values obtained for the fit are $r_c = 124$ kpc and $\beta = 0.5$ (see Table 7).

N79-299A illustrates the interesting dynamics which may contribute to HT formation in poor clusters. First, the relative velocity between NGC 4061 (associated with the NAT) and NGC 4065 (the compact radio source slightly to the East) is 850 km/s. This velocity is much greater than the expected $\sigma_v$ for a bound, poor cluster. Second, the optical isophotes of these two galaxies are distorted (Venkatesan *et al.* 1994) which may be indicative of a tidal interaction. The presence of the gas and the interaction between the two galaxies may have contributed to bending the jets, as discussed further in Sec. 5.

Figure 7(b) shows a fairly broad, flat velocity distribution. Based on the 24 galaxies plotted, the velocity dispersion is ~420 km/s.

Figure 8(b) shows the Zwicky chart associated with this region. Once again, the poor group is contained within a larger contour, which Zwicky classified as an open, near cluster.

*S49–128*: Figure 3(b) shows the twin jet radio source 4C 08.11 in S49–128, which may be a relaxed double or a wide-angle tailed (WAT) radio source (see, e.g., O'Donoghue *et al.* 1990). The optical identification is with the brightest galaxy at the apparent group center, NGC 1044. Fomalont *et al.* (1980) previously published a map of this source at 2.7 GHz. The source appears to be very similar to 3C 31 (Fomalont *et al.* 1980); also an FR Type I source in a poor cluster.

The compact, high surface-brightness X-ray peak and the compact radio core of 4C 08.11 are separated by 30″, within the expected position errors of the PSPC. Most of this emission is probably associated with NGC 1044. However, there is clearly diffuse X-ray emission around the extended radio source as shown in Fig. 3(a). The diffuse emission has a very clumpy, asymmetric shape. Several of the clumps appear to be associated with individual galaxies, indicated by the crosses on the figure. It is interesting to note that the radio jets broaden into diffuse lobes at the location where the X-ray surface brightness drops precipitously. The surface brightness profile was fit with a King model [Fig. 6(c)] with best-fit parameters $r_c = 75$ kpc and $\beta = 0.6$ (Table 7).

Figure 7(c) shows the velocity distribution for this cluster. Here a total of 16 galaxies are plotted. The velocity dispersion is 420 km/s. The velocity distribution appears broad and non-Gaussian.

Figure 8(c) shows the Zwicky chart for this cluster. S49-128 appears to be part of a much larger diffuse cluster classified as open and near by Zwicky *et al.* (1961–68).

*S49–132*: The radio source associated with NGC 7503 [shown in Fig. 4(b)] is another excellent example of a poor cluster NAT. The NAT does not coincide with the brightest X-ray peak in the cluster, but rather with a weak X-ray component to the East of the X-ray centroid. However, several weak, compact radio galaxies, of similar optical magnitude to NGC 7503 (see Table 5) do coincide with the dominant X-ray peaks. The overall X-ray morphology of this cluster, best shown in Fig. 4(a), is interesting. There is considerable diffuse X-ray emission which extends asymmetrically to the North–East and South of the X-ray peak.

Figure 6(d) shows the King model fit to the surface brightness profile. These parameters ($r_c = 243$ kpc, $\beta = 0.6$), as well as the X-ray luminosity ($2.5 \times 10^{43}$ ergs s$^{-1}$) and temperature ($kT = 2.3$ keV), are unusually large in comparison to the other poor clusters in our sample (see Table 7).

There were too few velocities in the literature to warrant showing the velocity distribution for this poor cluster. However, we have recently measured velocities for 23 galaxies associated with this cluster (which will be discussed in a future paper). The velocity distribution is quite unusual, remarkably flat, and broad. It is interesting to note that the velocities of the three Zwicky galaxies in this cluster are each separated by about 1000 km/s. This is clearly a complex dynamical system.

This poor cluster is projected onto the edge of Abell 2251. However, A2251 is a distance class 6 cluster, and the redshift of S49–132 implies that they are merely coincident by projection. But, Fig. 8(d) shows that S49–132 lies in the middle of a compact, near Zwicky cluster. The size and ex-

TABLE 7. X-ray properties of poor clusters.

| Cluster | $r_c^a$ | Extent[b] | $\beta$ | $kT^c$ | $n^d$ | $L_X^e$ | $M_{gas}^f$ | $M_{dyn}$ | $M_{VT}$ | $\tau^g$ | $\dot{M}^h$ |
|---|---|---|---|---|---|---|---|---|---|---|---|
| MKW2 | $67 \pm 18$ | 215 | $0.60 \pm 0.20$ | $1.24^{+2.41}_{-0.24}$ | 3.5 | $3.47^{+0.08}_{-0.06}$ | 0.02 | 1.96 | 2.64 | – | – |
| N79-299A | $124 \pm 5$ | 405 | $0.47 \pm 0.10$ | $0.82^{+0.20}_{-0.18}$ | 4.9 | $3.57^{+0.17}_{-0.14}$ | 0.18 | 1.47 | 3.73 | 2.50 | 0.20 |
| S49-128 | $75 \pm 4$ | 375 | $0.56 \pm 0.10$ | $0.85^{+0.20}_{-0.15}$ | 6.6 | $0.62^{+0.02}_{-0.02}$ | 0.17 | 2.02 | 1.05 | 7.85 | 0.22 |
| S49-132 | $243 \pm 8$ | 714 | $0.58 \pm 0.10$ | $2.10^{+0.80}_{-0.50}$ | 32.0 | $15.00^{+0.30}_{-0.40}$ | 1.67 | 6.85 | 18.00 | 1.10 | 1.37 |
| S49-140 | $91 \pm 9$ | 252 | $0.60 \pm 0.20$ | $1.04^{+0.20}_{-0.14}$ | 6.6 | $2.02^{+0.04}_{-0.08}$ | 0.12 | 1.60 | 2.80 | 0.60 | 0.16 |

[a] Core radius in kpc.
[b] Average radius in kpc to $2\sigma$ contour.
[c] Average temperature of ICM (keV).
[d] Number density of gas at the core ($10^{-4}$ cm$^{-3}$).
[e] X-ray luminosity $\times 10^{42}$ ergs s$^{-1}$ out to 0.33 Mpc, in the 0.44–2.04 keV band.
[f] All masses in $10^{13}$ $M_\odot$ ($M_{gas}$ and $M_{dyn}$ measured out to 0.33 Mpc).
[g] Central X-ray cooling times in $10^{10}$ yrs.
[h] Cooling mass accretion rate in $M_\odot$/yr.

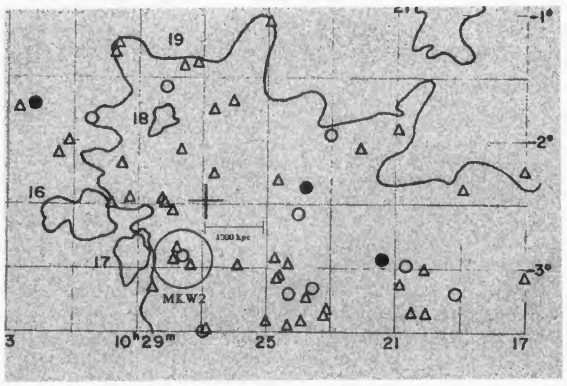


(a)

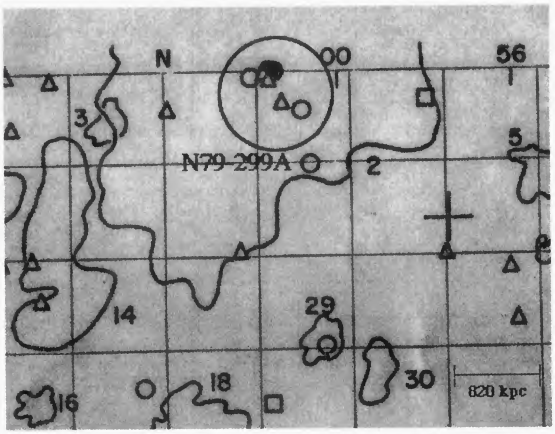


(b)

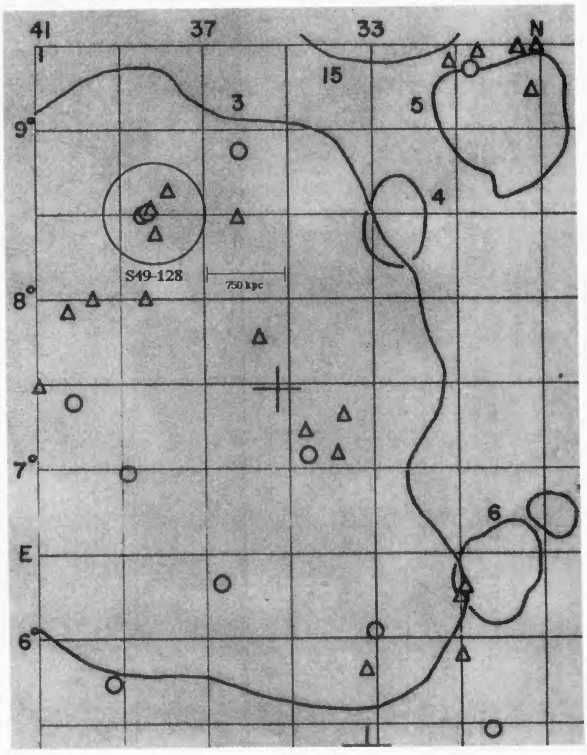


(c)

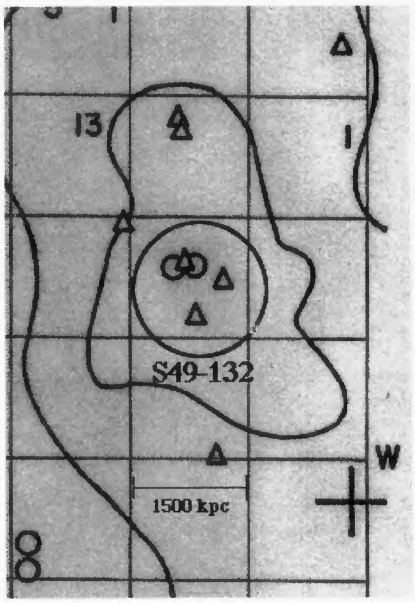


(d)

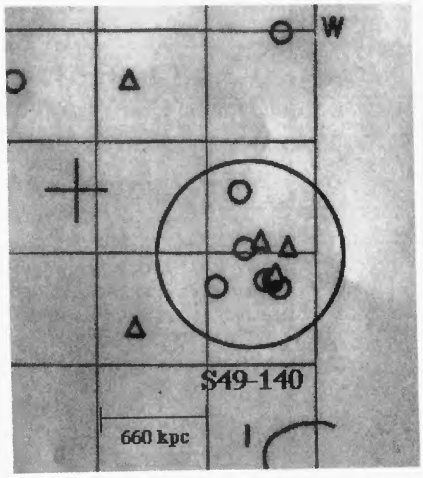


(e)

FIG. 8. (a)–(e) Zwicky maps for (a) MKW2, (b) N79-299A, (c) S49–128, (d) S49–132, and (e) S49–140, adapted from Zwicky *et al.* (1961–68). The Zwicky galaxies associated with the poor clusters are circled and the clusters are labeled. The linear scale at the distance of the cluster is also indicated. Note that only S49–140 does not fall within a Zwicky cluster.

tent of Zwicky's contour relative to the S49–132 group, coupled with the unusually large values of $r_c$, $L_X$, and $T$, suggests that this group may be a major part of a somewhat richer cluster.

*S49–140*: The tailed radio source [Fig. 5(b)] in S49-140 coincides with both NGC 741 and NGC 742. It is not clear which galaxy is actually the source of the radio emission, as the X-ray peak coincides with NGC 741, whereas NGC 742 appears to be at the head of the HT. Burns *et al.* (1981a) first noted this source in their survey of poor clusters with central

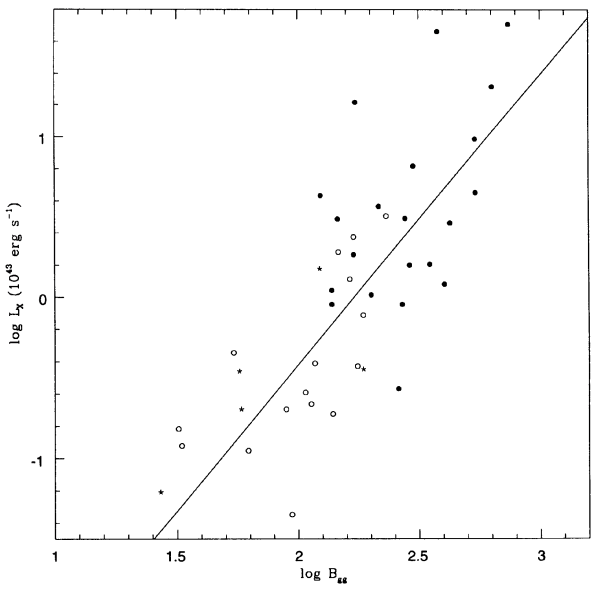


FIG. 9. The $L_X$ vs $B_{gg}$ relation for rich clusters (filled circles), poor clusters (open circles), and our poor clusters (asterisks), where $L_X$ was adjusted to the *Einstein* 0.5–4.5 keV band. The $x$ axis is the logarithm of $B_{gg}$, and the $y$ axis is the logarithm of $L_X$ in units of $10^{43}$ ergs/s. The solid line is the Price *et al.* fit for this relation.

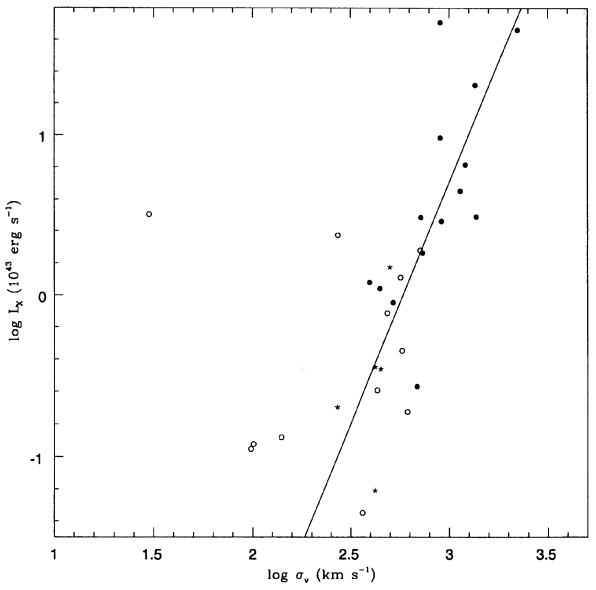


FIG. 10. The $L_X$ vs $\sigma_v$ relation for rich clusters (filled circles), poor clusters (open circles), and our poor clusters (asterisks), where $L_X$ was adjusted to the *Einstein* 0.5–4.5 keV band. The $x$ axis is the logarithm of $\sigma_v$, and the $y$ axis is the logarithm of $L_X$. The solid line shows the Price *et al.* fit for this relation.

dominant galaxies. Birkinshaw & Davies (1985) proposed that NGC 742 is superposed by chance on the hot spot of the source associated with NGC 741. However, due to the distortion in the optical morphology of NGC 742 (Davoust & Prugniel 1988; Prugniel *et al.* 1989), Venkatesan *et al.* (1994) suggested that NGC 742 is the source of the radio emission, possibly as a result of an interaction with NGC 741. If NGC 742 is the actual identification, then this radio source is a HT. However, if NGC 741 is the origin of the radio emission, the source should probably be classified as a relaxed, but distorted double. The radio map displayed in Fig. 5(b) is from Venkatesan *et al.* (1994).

Figures 5(a) and 5(b) show the clumpy, asymmetric X-ray emission within this cluster. Several of the X-ray clumps appear to be associated with individual galaxies. The surface-brightness profile [Fig. 6(e)] may be consistent with the presence of a cooling flow, but we have insufficient S/N to measure a separate core and diffuse gas temperature. We derived values of $r_c = 91.9$ kpc and $\beta = 0.60$.

Figure 7(d) shows the velocity distribution for 14 galaxies in this cluster. This distribution appears to be very Gaussian in shape. The velocity dispersion is ~270 km/s.

Figure 8(e) shows the Zwicky chart for this region of the sky. Of our five clusters, this is the only one which is not associated with a larger, diffuse cloud of galaxies. This cluster also has the lowest-velocity dispersion of the five clusters, and the most Gaussian of the velocity distributions. This is an interesting correlation. We discuss the significance of the larger-scale structure surrounding these groups in Sec. 5.2.

## 4. CLUSTER PROPERTIES

The new *ROSAT* observations of the poor groups reported in this paper present us with an opportunity to examine the general properties of these clusters. In the X ray, we have found that the poor clusters have emission that is not particularly well fit with the standard isothermal King model. In the optical, we have found that four of our poor clusters reside within larger groups identified by Zwicky *et al.* (1961–68). The velocity distributions may suggest unusual dynamical activity within some of these poor clusters. Finally, the presence of HTs may also be another indicator of unusual dynamics in these clusters.

In this section, we discuss the properties of these clusters and make comparisons to other poor clusters and to rich clusters. We consider relations between the X-ray luminosity, cluster richness, velocity dispersion, and temperature. The relation between the minimum pressure inferred from the radio and the thermal pressure measured from the X-ray surface brightness profile is examined. We also calculate the cluster masses, their baryonic fractions and mass inflow rates for the clusters which may have cooling flows.

### *4.1 Continuum of Rich and Poor Cluster Properties*

Several authors (e.g., Price *et al.* 1991) have suggested that a continuity of properties exists between rich and poor clusters. For example, many poor cluster properties ($L_X, T_{gas}, r_c, \sigma_v$) have values that lie between those of rich clusters and individual galaxies. Basic optical properties such as richness also seem to scale from poor to rich clusters. Poor clusters may provide a low mass extension to rich clusters, and can be used to study relations derived for rich clus-

ters. Our new detailed *ROSAT* observations allow us to probe this transition from rich to poor clusters in more detail.

The relationship between richness and $L_X$ has been studied for rich clusters (Abramopoulous & Ku 1983) and for poor clusters (Bahcall 1980). Price *et al.* (1991) combined Bahcall's data with the data on rich clusters to extend the relationship to lower $L_X$. In Fig. 9, we show a similar but new relation involving $L_X$ and $B_{gg}$, the coefficient of the spatial correlation function. The value of $B_{gg}$ is related to the over or under density of galaxies within a given volume, and thus can be used as a measure of the richness. Andersen & Owen (1994) measured $B_{gg}$ for a sample of Abell clusters and a subsample of the poor clusters from Burns *et al.* (1987). Following Anderson and Owen's prescription, we determined $B_{gg}$ for three of our poor clusters which were not in their paper. The filled circles in Fig. 8 denote Abell clusters, the open circles denote poor clusters, and the asterisks are the values for our poor clusters. The X-ray luminosities were taken from Price *et al.* and from our own measurements (for the poor clusters) and Jones and Forman (for the rich clusters). For our poor clusters, we corrected $L_X$ to the *Einstein* energy band (0.5–4.5 keV) and to a radius of 0.33 Mpc. (This correction can be carried out easily within the PROS task 'XFLUX,' which uses the best-fit Raymond–Smith spectral model to calculate X-ray flux and luminosity for a given range in energy. Thus, the *Einstein* energy band is used as one of the parameters in this task, in place of the *ROSAT* band.) It should be noted that there is considerable overlap between the two samples, indicating continuity between the rich and poor clusters. Also, the slope of the least-squares fit to the data (indicated by the solid line) is $1.86\pm0.33$, where Price *et al.* find the slope of the relation between $L_X$ and richness to be $1.90\pm0.26$. Since we use $B_{gg}$ here as a measure of cluster richness, this agreement is encouraging.

In Fig. 10, we plot $L_X$ vs $\sigma_v$ for Abell clusters (filled circles), poor clusters from Price *et al.* (open circles), and our five poor clusters (asterisks). (The velocity dispersions of our five poor clusters were calculated using published velocities. Two of these clusters, MKW2 and N79-299A, were studied by Dell'Antonio *et al.* (1994), who found velocity dispersions consistent with those listed in Table 5.) Price *et al.* find the slope of this relation to be $2.8\pm0.4$. We find a slope of $3.0\pm0.5$. Within the errors, these fits both agree with Quintana & Melnick (1982) who predict a slope of 3 for this relation. Figures 9 and 10 suggest that rich and poor clusters share a continuum of properties. This may imply that poor clusters are real physical systems, and not merely due to projection effects (see Sec. *5.1*).

### *4.2 Mass Determinations*

We calculated both the gas masses and dynamical masses for these five clusters using the deprojected ICM density profile. The gas mass was found by integrating this density profile out to a radius of 0.33 Mpc, which is about the radius at which the extended X-ray emission melds into the background. The total distribution of mass was also estimated

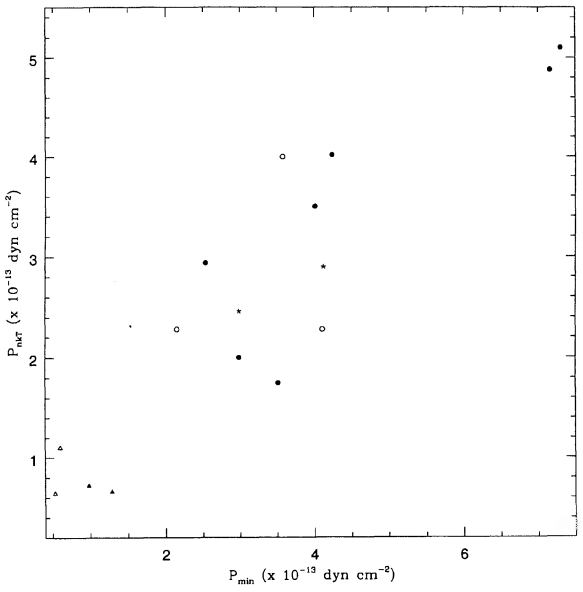


FIG. 11. Minimum pressure vs thermal pressure for MKW2 (filled triangles), N79-299A (open triangles), S49–128 (filled circles), S49–132 (open circles), and S49–140 (asterisks).

from the density profile. If the gas is in hydrostatic equilibrium, and is bound to the cluster potential (Sarazin 1986), then the total mass within some radius $r$ is

$$M(r) = -\frac{kT}{G\mu m_p}\left[\frac{d(\ln \rho_g)}{d(\ln r)} + \frac{d(\ln T)}{d(\ln r)}\right] r. \quad (4)$$

In most cases, we only had enough counts to derive one mean temperature for each cluster. Therefore, the temperature gradient was set to zero. For S49–132, we did have enough information to construct a temperature profile, and we did find that profile to be consistent with isothermal ICM gas. $M(r)$ is very sensitive to small variations between adjacent bins, so we used a smoothed density profile. We have calculated total masses of $0.5\text{–}1.0\times10^{14}$ $\mathcal{M}_\odot$, and gas masses of $0.1\text{–}2.0\times10^{13}$ $\mathcal{M}_\odot$, for these clusters as shown in Table 7. Thus, we find that for our clusters the ratio of X-ray luminous to total mass varies between 1% and 25%. A mass ratio of ~10% is consistent with that measured for many rich clusters (e.g., Edge & Stewart 1991). Mulchaey *et al.* (1993) measured a 4% baryonic fraction for the NGC 2300 poor group. However, Henriksen & Mamom (1994) found that the NGC 2300 group has a baryonic fraction of about 20%. Henriksen and Mamon note that the dependence of a baryonic fraction with a radius is not well constrained, partly because of uncertainties in estimating the background. (This is one instance showing the importance of determining the background as accurately as possible, which we have tried to do using the specific X-ray modeling techniques described in Sec. 3.)

These mass-calculations implicitly assume that the gas is in a state of hydrostatic equilibrium. However, in Sec. 5 we hypothesize that these clusters may not, in fact, be consistent with hydrostatic equilibrium. What impact does this have on our mass estimates? From numerical hydro/*N*-body simula-

tions (Roettiger *et al.* 1995), we may be overestimating the baryonic mass fraction by ~30%. This figure is based on numerical simulations of the early stages of mergers, in which the actual mass associated with the cluster particles (known prior to running the simulation) is compared to the mass calculated making the assumption of hydrostatic equilibrium.

We have also calculated the Virial mass for these clusters. Assuming spherical symmetry, the Virial mass is

$$M_{VT}=\frac{3\pi}{G}\sigma_R^2\left\langle\frac{1}{r}\right\rangle^{-1}, \quad (5)$$

where $\langle 1/r\rangle^{-1}$ is the mean harmonic radius (Oegerle & Hill 1994) and $\sigma_R$ is the radial velocity dispersion. The gas, dynamical, and Virial masses for each cluster are listed in Table 7.

### *4.3 Minimum Pressures and Thermal Pressures*

We have calculated the minimum pressure parameters for the diffuse radio emission components in these clusters, as well as the thermal pressure estimated from the X ray, to determine if the lobes are thermally confined. The minimum pressure equations (e.g., Burns *et al.* 1979; O'Donoghue *et al.* 1990) were used to calculate the minimum pressure magnetic field and the total pressure from the relativistic particles and the magnetic field. We assumed a uniform volume filling factor and magnetic fields transverse to the line of sight. The synchrotron spectrum was calculated assuming a power law ($S_\nu \propto \nu^{-0.8}$) over a frequency range of 10 MHz to 100 GHz. We calculated the minimum pressure for a cylindrical volume with area proportional to the clean beam and assuming spherical symmetry so that the depth along the line of sight was equal to the width in the plane of the sky.

Thermal gas pressures for several locations across the radio sources were calculated by determining the distance from the center of the X-ray emission to the desired location on the radio feature, finding the density at that radius from the density profile, and calculating $P=\rho kT/\mu m_H=nkT$, with $T$ being the average ICM temperature. In Fig. 11, we plot minimum pressure vs thermal pressure. There is a good correlation between the two pressures. Given the assumptions and expected errors, our results are consistent with thermal pressure confinement by the observed ICM for these poor cluster radio sources. This result supports the contention that the radio source pressures can be used to estimate the thermal pressure of the immediate gaseous environs in poor clusters (Venkatesan *et al.* 1994).

### *4.4 Central X-Ray Emission*

Four of these poor clusters (N79-299A, S49–128, S49–132, and S49–140) have central X-ray luminosity excesses (above that for an extrapolated King model). We interpret these luminosity excesses as emission due to the central galaxies and not as excesses due to cooling flows for the following reasons.

First, the X-ray luminosity excesses are of the same order of magnitude as X-ray emission from galaxies. In the 0.5–4.5 keV band, elliptical galaxies typically have X-ray luminosities of $10^{39}$–$10^{42}$ erg s$^{-1}$ (Canizares *et al.* 1987).

Second, for S49–132 there were sufficient counts to measure a temperature profile. Within the errors, the profile is consistent with a single temperature of 1.6 keV. For the other clusters, we have only obtained one temperature, due to low numbers of counts, and were forced to rely on the deprojected temperature profiles.

Third, the cooling times of the cluster cores are long. The thermal cooling time of the cluster core can be approximated by (Sarazin 1986)

$$\tau_{\rm cool}=8.5\times10^{10}\left(\frac{n_e}{10^{-3}\ {\rm cm}^{-3}}\right)^{-1}\left(\frac{T}{10^8\ {\rm K}}\right)^{1/2}\ {\rm yr}. \quad (6)$$

The cooling times are listed in Table 7. In two cases (N79-299A, S49–128), the cooling times are clearly longer than a Hubble time and thus rule out cooling flows in these clusters. In the other two cases (S49–132, S49–140), the cooling times are only slightly shorter than a Hubble time.

We have also calculated nominal mass inflow rates for the four clusters. The mass inflow rate is given by (Sarazin 1986)

$$\dot{M}=\frac{2}{5}\left(\frac{L_{\rm excess}}{kT}\right)\mu m_p, \quad (7)$$

where $L_{\rm excess}$ is the X-ray luminosity above that of the extrapolated King model in the core. The nominal mass inflow rates for these clusters are 0.2−1.4 $\mathcal{M}_\odot$/yr. Given these facts, we believe the central X-ray luminosity excesses are consistent with individual galaxy emission, and not due to cooling flows.

## 5. DISCUSSION

In this section, we present our interpretation of the many interesting features within these poor clusters. We discuss the possibility that systems identified as poor clusters may result from projection along a gas filament. We also present the ram pressure requirements for bending radio jets into HTs in greater detail. Finally, we hypothesize that poor clusters are dynamically young systems which have collapsed out of larger, loose aggregates of galaxies.

### *5.1 Are These Clusters Real Physical Systems?*

Mamon (1987) and more recently Hernquist *et al.* (1994) have suggested that Hickson compact groups may not be real physical systems but simply projections of galaxies along the line of sight. In particular, Hernquist *et al.* argue from their large-scale structure CDM numerical simulations that artificial compact groups can be created by projections of galaxies along long filaments, which are commonly found in such simulations. This would then eliminate the time scale and merging problems for these groups (e.g., Mamon 1987). Their arguments are relevant here since the poor clusters in this paper are similarly dense.

The distribution of galaxy velocities in 31 poor groups selected from the Burns *et al.* (1987) sample were recently reported by Dell'Antonio *et al.* (1994). They show a rela-

tively large range of velocities (13 of the groups have velocity dispersions in the range 300–1000 km/s). It is possible that what appears to be a poor group is in fact a number of galaxies associated with a long filament, viewed such that the filament axis is along the line of sight. Thus, an apparent poor group could actually be a number of unrelated galaxies viewed in projection, which could explain why some of the poor groups in the Dell'Antonio sample had velocity dispersions of up to 1000 km/s.

But, does the fact that each of the five clusters discussed in this paper have X-ray detections with core-halo morphologies rule out projections? In general, the X-ray properties reported in Sec. 4, including luminosities, core radii, and temperatures, are consistent with that expected for real groups of galaxies. The properties of these poor clusters seem to form the lower mass extension of the rich clusters. However, could these X-ray properties also be produced by projections of X-ray emission along galaxy/gas filaments? To address this question, we analyzed the filamentary gas structure in a new hydro+$N$-body simulation of a CHDM universe (Bryan *et al.* 1994; Loken *et al.* 1995). The X-ray emission from this (113 Mpc)$^3$ volume at the present epoch was projected in various directions to "observe" the cluster/group surface brightness with the same sensitivity as *ROSAT*. Poor clusters were identified in both the three-dimensional (3-D) and then in the projected 2-D area. The two lists of groups agreed extremely well. There were few, if any, artificial poor clusters produced by projection of X-ray gas along filaments. In general, the filaments were too cool ($T<8\times10^6$ K) and tenuous ($\sim10^{-5}$ cm$^{-3}$) to produce "fake" clusters.

Furthermore, the presence of head–tail radio galaxies in these regions argues against these poor clusters being strictly projection effects. If the radio galaxies were simply part of the galaxy filament, and not associated with a denser group, they would be embedded within the average gas properties of the filament. The filament gas pressure is <1% of that at the cores of the poor clusters if they are real (Table 7). Furthermore, the ram pressure within the filaments is quite low due to the very low gas density and the small baryon velocity dispersion (<500 km/s). Following the Euler's equation analysis in Sec. *5.2*, it then becomes even more difficult to bend the jets to their observed curvature within a galaxy filament.

So, given the X-ray properties of the poor clusters and the presence of head–tail sources, we believe that these are real, physical systems.

### *5.2 Bending Poor Cluster NATs*

Throughout this paper, we have stated that the bent jets of poor cluster NATs are of interest because velocities ~1000 km/s are required for ram pressure to be effective. It was thought that such velocities are not consistently found within poor clusters. Let us now examine this velocity requirement in more detail.

Consider a radio source moving through an ICM of mass density $\rho_{\rm ICM}$ with galaxy velocity $v_g$. The bending of a laminar fluid jet associated with a NAT is described by the relativistic, time-independent Euler's equation given by (see, e.g., O'Dea 1985)

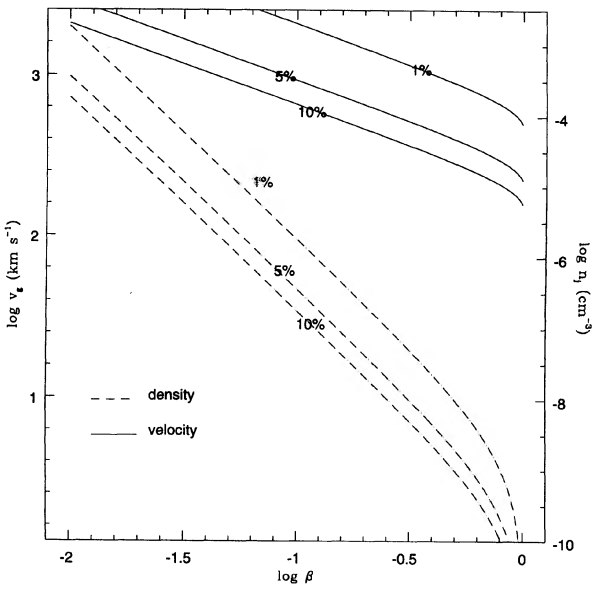


FIG. 12. Galaxy velocity and number density as a function of $\beta$, the speed of the jet material. $v_g$ is the velocity of the radio galaxy relative to the ICM and $n_j$ is the density of the jet material. The efficiency of the conversion of jet energy to radio luminosity, $\epsilon$, is indicated by the percentages attached to each curve.

$$\frac{w_j\gamma^2\beta^2}{R}\approx\frac{\rho_{\rm ICM}v_g^2}{h}, \tag{8}$$

where $w_j=\rho_jc^2+U_{\rm int}+P_{\rm int}$ is the relativistic enthalpy per unit volume along a jet of density $\rho_j$, $\beta=v_j/c$, $\gamma=(1-\beta^2)^{-1/2}$, $h$ is the scale length over which the ram pressure is exerted, and $R$ is the radius of curvature of the jet. For a so-called "cold" jet (i.e., one with Mach number $\gg1$), one can assume that the internal energies of the jet are small compared to the bulk kinetic energy. Thus, $w_j\approx\rho_jv_j^2$ and Euler's equation becomes

$$\frac{\rho_jv_j^2\gamma^2}{R}\approx\frac{\rho_{\rm ICM}v_g^2}{h}. \tag{9}$$

To constrain some of the parameters in Eq. (9), we assume that the energy of the jet is converted to the observed radio luminosity $L_{\rm rad}$ with some efficiency $\epsilon$. Thus, for a jet of radius $r_j$, mass density $\rho_j$, and bulk flow velocity $v_j$, and

TABLE 8. Radio jet parameters for NGC 4061 in N79-299A.

again neglecting the internal energies of the jet, the radio luminosity can be described by

$$L_{\rm rad} \approx \epsilon \pi r_j^2 \rho_j c^2 \gamma(\gamma-1)\left(\frac{r_{ji}}{r_{jf}}\right)^{2/3}, \quad (10)$$

where $r_{ji}$ is the initial jet radius and $r_{jf}$ is the final jet radius. We will assume that the efficiency with which the jet energy is converted to radio luminosity ($\epsilon$) is constant along the jet.

From Eqs. (9) and (10), we solve for $v_g$ the velocity of the radio source with respect to the ICM needed to bend the jet, such that

$$v_g \approx \sqrt{\frac{L_{\rm rad}\beta\gamma h}{(\gamma-1)\rho_{\rm ICM}\epsilon\pi r_j^2 cR}\left(\frac{r_{ji}}{r_{jf}}\right)^{2/3}}. \quad (11)$$

The advantage to this formulation is that we need not consider $\rho_j$, which is not well constrained; instead, $v_g$ depends on as many observable quantities as possible (although we must still make some assumptions for $\beta$ and $\epsilon$).

In Fig. 12, we show plots of $v_g$ and jet number density vs $\beta$ for the case of N79-299A. The observable quantities used for this calculation are shown in Table 8. In this formulation, the jets become "stiffer" at lower jet velocities (since $\rho_j \propto (v_j\gamma(\gamma-1))^{-1}$) and require higher galaxy velocities to bend to the observed radius of curvature. The jet becomes very tenuous ($<10^{-6}$ cm$^{-3}$) at relativistic velocities, and may quickly disrupt via Kelvin–Helmholtz instabilities. So, for efficiencies between 1%–10% and jet densities $>10^{-6}$ cm$^{-3}$, we find $v_g$ must be of order 1000 km/s to produce appreciable bending of the jets. This also implies jet velocities $\leq 0.03c$.

### *5.3 Are These Poor Clusters Dynamically Young?*

These five clusters have extended, HT radio sources, and we have taken the presence of these HTs as one indication that these poor groups are real, physical systems. Although it is now known that HTs are found in poor clusters, it is difficult to account for their presence unless these galaxies have 3-D velocities relative to the ICM gas of ~1000 km/s. If these poor clusters are bound systems, then the HTs should not have such high velocities. Yet, some poor groups do exhibit very high relative velocities between group members (e.g., NGC 4061 and NGC 4065 in N79-299A, which have a relative line-of-sight velocity of ~850 km/s, and the three Zwicky galaxies in S49-132, with $\Delta v \approx 1000$ km/s). Also, our X-ray observations have shown that these poor clusters have clumpy, asymmetric gas distributions, with the clumps often coinciding with subgroups of galaxies.

How can we understand the interesting, diverse properties of these groups, especially the appearance of HT radio sources? One possibility is that these poor clusters have undergone recent, dynamically interesting activity—i.e., that these poor clusters have recently coalesced or collapsed out of large, loose "clouds" of galaxies. Such poor clusters would resemble relatively compact groups embedded within diffuse associations of galaxies.

HTs seem to occur with the same frequency in rich and poor clusters. But if poor clusters are relaxed, then it was expected that HTs would occur less frequently in poor clusters than in rich clusters. However, within a dynamically young poor cluster, the galaxies would not have had time to form a relaxed system, and the gas might still be turbulent and not yet in a state of hydrostatic equilibrium. The velocities of the galaxies would reflect that of the larger-scale system. Thus, radio galaxies passing near the core of the cluster for the first time could experience velocities relative to the gas of 1000 km/s, and so experience sufficient ram pressure to bend radio jets into HT morphologies.

For such dynamically young systems, one would expect a broad distribution of galaxy velocities. Here, we turn to recent numerical simulations of compact group formation for insight. Diaferio *et al.* (1993) have recently performed $N$-body simulations of compact group formation. They find that a significant fraction of recently collapsed groups have velocity dispersions in the range 300–1000 km/s. The larger dispersion systems, in particular, have non-Gaussian velocity distributions. Recently, Dell'Antonio *et al.* (1994) published velocity distributions for a number of poor clusters chosen from the same sample (Burns *et al.* 1987) as our clusters. Many of these clusters have velocity distributions (broad and flat) resembling those in the above $N$-body models. Out of 31 clusters, 13 have velocity dispersions between 300 and 900 km/s. Figures 7(a)–7(d) show that some of these poor clusters have interesting, broad velocity distributions, and our own spectroscopic observations (to be published in a paper in preparation) reveal that the velocity distribution of S49-132 also has an unusual distribution of velocities. So, both observations and simulations indicate that poor clusters can have very broad velocity distributions, and such distributions are expected for dynamically young systems. HTs may be a signal that the cluster is a system with an unusual velocity distribution.

Poor clusters that have recently collapsed should still be embedded within large, loose clouds of galaxies. Figures 8(a)–8(e) show the Zwicky *et al.* charts for these five poor clusters. Of the five clusters, four are embedded within larger low-density "clouds" of galaxies. The exception is S49–140, which has the lowest $\sigma_v$ of our five clusters, and the most Gaussian-like velocity distribution. The $N$-body simulations of Diaferio *et al.* suggest that compact groups are continually forming out of large, loose aggregates of galaxies. Thus, while the mean lifetime of their simulated groups is about 1 Gyr, new compact systems replace the older ones, explaining why compact groups are observable today. Also, Ramella *et al.* (1994) have studied the neighborhoods of 38 Hickson (1982) compact groups (HCGs) using the CfA red-shift survey. Of these 38 HCGs, 29 were found within larger clouds of galaxies that Ramella *et al.* called "HCG associations." Our poor clusters are generally as compact as HCGs, so such models may be applicable here as well. The presence of four of our poor clusters within large Zwicky clusters is understandable if they are dynamically young systems which have recently collapsed out of larger galaxy systems. This suggests that the Zwicky open clusters, none of which are in the Abell (1958) catalog, are real and are important incubators of galaxy groups.

## 6. CONCLUSIONS

In this paper, we have presented the results of deep *ROSAT* pointed observations of five poor clusters. Although we have detected extended X-ray emission from the ICM in all these groups, we note that the X-ray emission associated with these clusters is generally quite clumpy and asymmetrical. The clumps are often associated with subgroups of galaxies or individual galaxies, as well as with radio sources, and this may indicate that the gas is not yet in a state of hydrostatic equilibrium. These observations are consistent with Burns *et al.* (1994a), who found a strong correlation between ICM X-ray emission clumps and radio galaxies.

There are several additional results that we wish to emphasize. First, the observed ICM densities in these clusters, when coupled with sufficiently large galaxy velocities relative to the gas, may provide enough ram pressure to bend the observed radio jets/tails into the head–tail morphology. Also, the thermal pressures in the cluster ICMs are sufficient to confine the extended tails or lobes. Interestingly, the lobes/tails generally flare out in diameter in low X-ray surface brightness regions. Second, some of these galaxies (such as NGC 4061, within N79-299A) show signs of interesting interactions with neighboring galaxies, which may also be indicative of young clusters. Third, four of these five clusters are embedded within larger Zwicky cluster contours. This may indicate that Zwicky's open clusters are in fact real systems and provide important "nesting grounds" for compact groups. So, while we find a strong continuity in many X-ray (e.g., $L_X$, $r_c$, and $\beta$) and optical (e.g., $\sigma_v$ and $B_{gg}$) properties between our galaxy groups and rich Abell clusters, their other properties (velocity distributions, presence in low-density Zwicky clusters, and detailed X-ray morphology) are consistent with their being evolving, collapsing systems. Fourth, we find baryonic fractions on the order of 1% to 25%, similar to that in rich clusters, although the uncertainties may be >2. Fifth, some poor clusters (e.g., N79-299A, S49–128, and S49–132) have velocity distributions suggestive of unrelaxed systems. These distributions may reflect the velocities associated with larger-scale systems (i.e., Zwicky clusters). Thus, *we hypothesize that these poor clusters have recently collapsed out of large, loose clouds of galaxies.*

Our group is involved in projects to investigate this hypothesis further, which include constructing the first X-ray luminosity function for poor clusters from the *ROSAT* All-Sky Survey, gathering detailed velocity distributions for a sample of poor clusters using multifiber spectroscopic observations, and multicolor CCD imaging.

This work has been supported by a NASA Long Term Space Astrophysics grant (No. NAGW-3152), a *ROSAT* data analysis grant (No. NAG5-1819), and National Science Foundation grant (No. AST-9317596) to JOB. We thank Steve Snowden for making a $\beta$-release version of his software available to us. We acknowledge the PROS team at SAO for their helpful advice, the NRAO for its AIPS software, and the NASA GSFC for its XSPEC software. We have made use of the NASA/IPAC Extragalactic Database (NED) which is operated by JPL, Cal Tech, under contract with NASA. We have also made use of NASA's Astrophysics Data System (ADS) v4.0. We thank Chris Loken for help with the supercluster filament analysis, Kurt Roettiger and Jason Pinkney for many fruitful discussions, T. Venkatesan for assistance with the new VLA images, and the referee for several helpful comments.

## REFERENCES

Abell, G. O. 1958, ApJS, 3, 211
Abramopoulous, F., & Ku, W. H.-M. 1983, ApJ, 271, 446
Albert, C. E., White, R. A., & Morgan, W. W. 1977, ApJ, 211, 309
Anderson, V., & Owen, F. N. 1994, AJ, 108, 361
Arnaud, K. A. 1988, in Cooling Flows in Galaxies and Clusters, edited by A. Fabian (Cambridge University Press, Cambridge), p. 31
Auriemma, C. G., Perola, G., Ekers, R., Fanti, R., Lari, C., Jaffe, W., & Ulrich, M. 1977, A&AS, 57, 41
Bahcall, N. A. 1980, ApJ, 238, 117
Bevington, P. R. 1969, Data Reduction and Error Analysis for the Physical Sciences (McGraw-Hill, New York)
Birkinshaw, M., & Davies, R. L. 1985, ApJ, 291, 32
Burns, J. O., Owen, F. N., & Rudnick, L. 1979, AJ, 84, 1683
Burns, J. O., White, R. A., & Hough, D. H. 1981a, AJ, 86, 1
Burns, J. O., Gregory, S. A., & Holman, G. D. 1981b, ApJ, 250, 450
Burns, J. O., Hanisch, R. J., White, R. A., Nelson, E. R., Morrisette, K. A., & Moody, J. W. 1987, AJ, 94, 587
Burns, J., Rhee, G., Roettiger, K., Pinkney, J., Loken, C., Owen, F., & Voges, W. 1994a, The First Stromlo Symposium: The Physics of Active Galaxies, edited by G. Bicknell and P. Quinn, PASP Conf. Series, 54, 325
Burns, J., Roettiger, K., Pinkney, J., Loken, C., Doe, S., Owen, F., Voges, W., & White, R. 1994b, The Soft X-ray Cosmos, edited by E. Schlegel, and R. Petre (AIP, New York), p. 183
Burns, J. O., Rhee, G., Owen, F. N., & Pinkney, J. 1994c, ApJ, 423, 94
Butcher, J. A., & Stewart, G. C. 1991, in NATO Advanced Study Institute, Clusters and Superclusters of Galaxies, edited by M. M. Colless, A. Babul, A. C. Edge, R. M. Johnstone, and S. Raychaudhury (Kluwer, Dordrecht), p. 25
Bryan, G. L., Klypin, A., Loken, C., Norman, M. L., & Burns, J. O. 1994, ApJL, 437, L5
Canizares, C. P., Fabbiano, G., & Trinchieri, G. 1987, ApJ, 312, 503
David, L. P., Jones, C., Forman, W., & Daines, S. 1994, ApJ, 428, 544
Davoust, E., & Prugniel, P. 1988, A&A, 201, L30
Dell'Antonio, I. P., Geller, M. J., & Fabricant, D. G. 1994, AJ, 107, 427
Diaferio, A., Ramella, M., Geller, M. J., & Ferrari, A. 1993, AJ, 105, 2035
Dressler, A. 1984, ARA&A, 22, 185
Edge, A., Stewart, G., Fabian, A., & Arnaud, K. 1990, MNRAS, 245, 559
Edge, A. C., & Stewart, G. C. 1991, MNRAS, 252, 414
Eilek, J. A., Burns, J. O., O'Dea, C. P., & Owen, F. N. 1984, ApJ, 278, 37
Fabian, A. C. 1994, ARA&A, 32, 277
Fanaroff, B. L., & Riley, J. M. 1974, MNRAS, 167, 31
Fanti, R. 1984, in Clusters and Groups of Galaxies, edited by F. Mardirossian, G. Giuricin, and M. Mezzeti (Reidel, Boston), p. 185
Fomalont, E. B., Bridle, A. H., Willis, A. G., & Perley, R. A. 1980, ApJ, 237, 418
Gorenstein, P., Fabricant, D., Topka, K., Harnden, F. R., & Tucker, W. H. 1978, ApJ, 224, 718
Helou, G., Madore, B. F., Schmitz, M., Bicay, M. D., Wu, X., & Bennett, J. 1991, in Databases and On-Line Data in Astronomy, edited by D. Egret and M. Albrecht (Kluwer, Dordrecht), p. 89
Hernquist, L., Katz, N., & Weinberg, D. H. 1994, preprint
Henriksen, M. J., & Mamon, G. A. 1994, ApJL, 421, L63
Hickson, P. 1982, ApJ, 255, 382

Huchra, J. P., & Geller, M. J. 1982, ApJ, 257, 423
Jaffe, W., & Gavazzi, G. 1986, AJ, 91, 204
Jones, C., & Forman, W. 1984, ApJ, 276, 38
King, I. 1962, ApJL, 174, L123
Kriss, G. A., Cioffi, D. F., & Canizares, C. R. 1983, ApJ, 272, 439
Ledlow, M. J. 1994, Ph.D. thesis, University of New Mexico
Ledlow, M. J., & Owen, F. N. 1995, AJ 109, 853
Loken, C., Klypin, A., Burns, J., Bryan, G., & Norman, M. 1995, in preparation
Mamon, G. A. 1987, ApJ, 321, 622
Morgan, W. W., Kayser, S., & White, R. A. 1975, ApJ, 199, 545
MPE 1991, ROSAT AO2 Call for Proposals
Mulchaey, J. S., Davis, D. S., Mushotzky, R. F., & Burstein, D. 1993, ApJL, 404 L9
O'Dea, C. P. 1985, ApJ, 295, 80
O'Dea, C. P., & Owen, F. 1986, ApJ, 301, 814
O'Donoghue, A. A., Owen, F. N., & Eilek, J. A. 1990, ApJS, 72, 75
Oegerle, W. R., & Hill, J. M. 1994, AJ, 107, 857
Pildis, R. A., Bregman, J. N., & Evrard, A. E. 1995, ApJ (in press)
Ponman, T., & Bertram, D. 1993, Nature, 363, 51
Price, R., Burns, J. O., Duric, N., & Newberry, M. 1991, AJ, 102, 14
Prugniel, P., Davoust, E., & Nieto, J.-L. 1989, A&A, 222, 5
Quintana, H., & Melnick, J. 1982, AJ, 87, 1
Ramella, M., Diaferio, A., Geller, M. J., & Huchra, J. P. 1994, AJ, 107, 1623
Roettiger, K., Loken, C., & Burns, J. 1995, in preparation
Saracco, P., & Ciliegi, P. 1995, A&A (in press)
Sarazin, C. L. 1986, Rev. Mod. Phys., 58, 1
Snowden, S. L., McCammon, D., Burrows, D. N., & Mendenhall, J. A. 1994, ApJ, 424, 714
Stark, A. A., Gammie, C. F., Wilson, R. W., Bally, J., Linke, R. A., Heiles, C., & Hurwitz, M. 1992, ApJS, 79, 77
Turner, E. L., & Gott, J. R. 1976 AJ, 91, 204
Venkatesan, T. C. A, Batuski, D. J., Hanisch, R. J., & Burns, J. O. 1994, ApJ, 436, 67
White *et al.* 1995, in preparation
Zwicky, F., Herzog, E., Karpowicz, M., Kowal, C. T., & Wild, P. 1961–68, Catalogue of Galaxies and Clusters of Galaxies (California Institute of Technology, Pasadena)